CHAPTER 8

Hot gas path heat transfer characteristics/ active cooling of turbine components

T. Simon[1] & J. Piggush[2]
[1]*Department of Mechanical Engineering, University of Minnesota, USA.*
[2]*Pratt and Whitney, Inc., USA.*

Abstract

Gas turbines play an important role in the lives of all of us. They are instrumental in providing electricity or fuel to our homes and in transportation via aircraft and ships. Despite over 50 years of operation and their current ubiquity, gas turbines continue to evolve, becoming more fuel efficient, reliable, and durable. With present emphasis on further improvement in efficiency and operation with alternative fuels, significant engineering challenges remain. The gas turbine did not come about by virtue of a single, momentous breakthrough, but rather by numerous small advances on many fronts, including heat transfer, aerodynamics, materials, dynamics, lubrication, and fuels. The efforts of tens of thousands of engineers have produced the present, extensive body of knowledge that provides our basis for further development. Given the complexity of the engine, it is quite easy to become overwhelmed when trying to become acquainted with the technology on which it is based. This chapter is offered to help in one aspect of gas turbine technology, the gas path heat transfer within the turbine. It aims first to describe the physics of engine heat transfer by developing from simple ideas an introduction to the complex heat transfer phenomena within. This effort attempts to address how the engineer applies heat transfer tools available in the literature to support designs, which will advance engine life and enhance efficiency. If successful, the newcomer will establish a foothold in the technology and the more experienced engineer will be reminded of some basic concepts.

1 Introduction

The main objective sought by the gas turbine heat transfer engineer is to provide an airfoil and gas path design, which is both efficient and can meet the life

WIT Transactions on State of the Art in Science and Engineering, Vol 42, © 2008 WIT Press
www.witpress.com, ISSN 1755-8336 (on-line)
doi:10.2495/978-1-84564-062-0/08

goals. This requires a broad understanding of the system. First, an understanding of the constraints associated with the material to be used must be developed. This information (which is often proprietary and carefully protected) includes such parameters as the material maximum use temperatures associated with oxidation and corrosion life, creep, and thermal–mechanical fatigue (all functions of temperature and stress). Given the projected usage and life goals, the designer applies life equations to determine metal temperature limits throughout the airfoil and on the passage walls. The internal cooling and film cooling schemes are designed to maintain the metal temperatures below these limits.

The heat transfer engineer has several tools, which can be applied to provide a cooling scheme that meets the temperature constraints with minimal negative impact on engine aerodynamic and structural performance. These tools generally fall into two broad categories: those that cool the airfoil and endwalls inside and those that reduce the external heat load. Note that with regard to heat transfer from the passage flow to the airfoil, the two broad categories have opposite effects on heat transfer. Internal cooling generally increases airfoil surface heat transfer rates, while the external cooling aims to reduce them. They both tend to reduce airfoil and endwall temperatures. The complexity of choices to apply the various techniques to be discussed requires that the gas turbine heat transfer engineer has a thorough understanding of the entire heat transfer problem.

Internal cooling schemes generally employ one or more of the following techniques: impingement of cooling flow upon the wall to be cooled, convective cooling by channeling coolant flow through passages within the airfoil or endwall, and conduction through pin fin arrays to augment heat transfer within the solid components of the airfoil and enhance convection by increasing both flow turbulence and fluid-to-metal contact area. The choices for flow conditions and cooling path configurations associated with the cooling scheme are influenced by the pressure of the cooling flow supply, the temperature of the coolant fluid, the heat load distribution, and the stress distribution within the airfoil.

The external heat load may be controlled by one or more of the following methods. First, there is the geometry. Although the shape of the airfoil is generally defined by aerodynamic considerations, there are regions, such as the leading and trailing edges, where some improvements may be effected, while maintaining acceptable aerodynamic performance. As necessary to accommodate cooling, the airfoil is thicker than the aerodynamic design engineer would have it. Also, there are thermal barrier coatings (TBCs). These are generally ceramic-based coatings that have low thermal conductivity. They are used to reduce the heat flux through the airfoil wall. Finally, film cooling can be applied effectively on the external surface of the airfoil and on the endwall to reduce the temperature of the gas flowing immediately adjacent to the airfoil and endwall surfaces. It should be noted that film cooling injection into the gas path is usually done with an aerodynamic penalty. Effective cooling schemes must consider all impacts on the engine design.

Designers quickly realize that airfoil design is truly complex. The internal configuration has a direct influence on the external heat load distribution, while the external heat load defines what the internal thermal design must accomplish.

Finding the final configuration of the airfoil requires a systematic approach to the analysis; either beginning with the external heat load and then moving into the coolant fluid (the direction of energy flow) or beginning with the internal coolant and then documenting the external heat load (essentially moving in the general direction of the coolant). Although the choice is arbitrary, the discussion herein will move from the inside of the airfoil to the outside. As with any design process, multiple iterations through the analysis are required.

The thermal capacity of the coolant used for internal cooling is finite, defined by the mass flow rate, the coolant's specific heat, and the coolant temperature. The heat transfer engineer must carefully balance coolant flow rates and pressure drops while augmenting heat transfer coefficients with various devices to effect proper cooling. Figure 1 shows the arrangement of various coolant flows.

The external heat transfer situation is different. Energy flows past and into the airfoil from, effectively, an infinite source, the passage stream. The influence on passage energy flow of the airfoil's cool surface is minor. The main concerns are: (1) reducing the external effective heat loads between the airfoil wall or endwall and the bulk passage flow, and (2) reducing the external area. The heat transfer engineer has little opportunity to effect significant changes in the second concern. Film cooling offers the possibility of introducing a film of cooler fluid (spent from the internal cooling functions) to cover the external surface of the airfoil to help effect the first concern listed above. This film offers a cooler source temperature for convective heat transfer through the thermal boundary layer from the passage

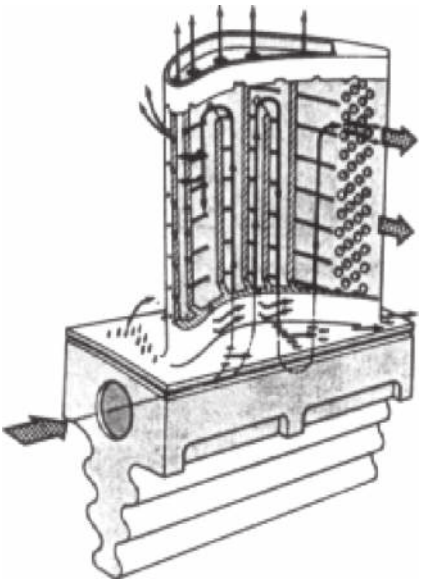

Figure 1: Coolant flows: internal channels in airfoil and endwall, impingement jets, trailing edge and tip region flows, film cooling flows (from NASA Glenn).

flow to the surface and, as such, reduces heat flux across the convective layer. Film cooling has, over the years, evolved to become a very effective method for reducing the airfoil and endwall surface temperatures. A second opportunity for reducing the surface heat flux is to introduce a solid-material coating of high thermal resistivity on the surface. This, in conjunction with the reduced heat flux due to film cooling and with effective internal cooling, gives lower temperatures on the airfoil external surfaces and load-bearing regions of the airfoil and endwall.

The internal geometries of high-performance engine airfoils tend to be very complex, incorporating many features designed to strategically cool the internals so that the entire external surface of the airfoil remains generally at a uniform temperature at a level, which is suitable for sustained operation. Complicating the problem is the matter of getting sufficient coolant supply pressure and in dealing with the thin trailing edge, the exposed tip, and the high heat transfer stagnation region at the leading edge of the airfoil. A rise in convective heat transfer coefficient in a channel flow by some devised method or another is generally accompanied by a rise in pressure drop, giving a trade-off between enhancement and flow rate. Cooling flow circuit designs optimize the distribution of cooling effectiveness for a given pressure drop. Manufacturing considerations, such as accommodating component thermal growth and maintaining clearances, as well as controlling cost (usually reflected in avoiding very fine feature sizes) are also taken into consideration. Designing a cooling scheme for a high performance engine gas path becomes a delicate balancing act between designs for internal and external heat transfer performance among many other design considerations. Tools include a strong fundamental understanding of flow and heat transfer and a working knowledge of the many other design considerations. Codes and design methods are available to the heat transfer engineer, but a fundamental understanding is paramount.

References, such as the excellent books by Han *et al.* [1] and Lakshminarayana [2] provide more detail to gas turbine heat transfer design and to turbomachinery design, respectively.

2 Hot gas path heat transfer characteristics

The flow entering the turbine gas path has come from the combustor, as shown in Fig. 2. Within the combustor, fuel (either a liquid similar to kerosene or diesel fuel or a gas, such as methane, syngas or high hydrogen and syngas (HSG) processed from coal) and air combine in a highly exothermic reaction that leads to high-temperature products of combustion at the high combustor pressure. A modern combustor called a dry, low-NO_x combustor operates lean and without water injection. A second type called a catalytic combustor has a selective catalytic reduction in the exhaust stream. In the low-NO_x combustor, excess air is used to maintain the combustor exit temperature at a suitable limit, consistent with the engine design and turbine durability limits. Combustor designs often have a strong swirl in the combustion zone to enhance mixing and shorten the reaction zone. About 30% of the airflow enters the primary combustion zone either through a swirl section, or through holes in primary zone of the combustion chamber. The remainder of

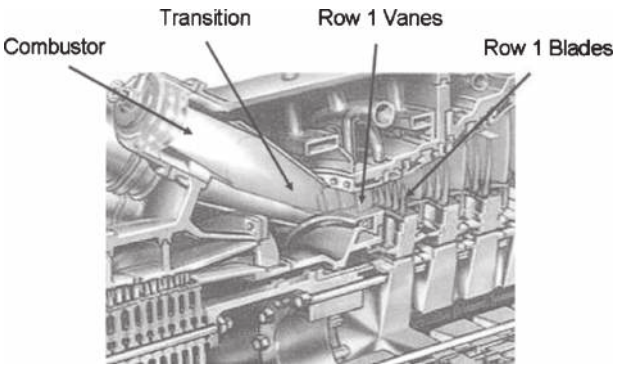

Figure 2: Hot gas path of a Siemens SGT6-5000F Gas Turbine (from Brummel *et al.* [3]).

the air, about 70% of the total airflow, is supplied through holes in the combustor liner as dilution air to mix and cool the flow and to protect the liner from reaching excessive temperature levels. In the case of a catalytic combustor, a catalytic reactor section is put downstream of the fuel/air mixing section of a pre-burner. This reactor consists of rather fine channels coated with a catalyst, such as palladium oxide. The catalytic reaction takes place at temperature levels that are below the turbine inlet temperature so a downstream combustor is needed to raise the gas temperature to the turbine inlet temperature. This combustor is similar to the dry low-NO_x combustor.

The flow passes from the combustor exit to the turbine through a transition section. This section generally has a decreasing area in the streamwise direction and some wall curvature, depending on the combustor and turbine designs. The flow departs the transition section to enter the vane section of the first stage turbine. To accommodate thermal growth of components, the junction between the transition section and the turbine is fabricated with gaps in the wall, see Fig. 3. These gaps are sealed against ingression of hot gases with compressor discharge air that has been routed through a cavity in the centre of the engine.

The flow then is turned through the vane, or nozzle, row of the first stage of the turbine. In this row, the flow is given a swirl (a circumferential velocity component) and is accelerated to a higher velocity. With the rise in velocity, there is a drop in static temperature of the passage flow. This temperature change in the passage core flow can be estimated by analyzing it as a one-dimensional isentropic flow. Local velocities within the vane row can be at sonic velocity or mildly supersonic and shock waves can stand within the passage. Generally, a shock from the trailing edge of one vane crosses the passage to impinge on the suction surface of the neighboring vane. This shock will affect wall heat transfer rates on the suction surface at the location of impingement, and downstream. The fluid temperature upon entry to the vane row exceeds the maximum allowable materials temperature; thus, this row must be aggressively cooled. The gas path heat transfer engineer spends most of their time on the design of the first stage vane and rotor sections. The techniques for

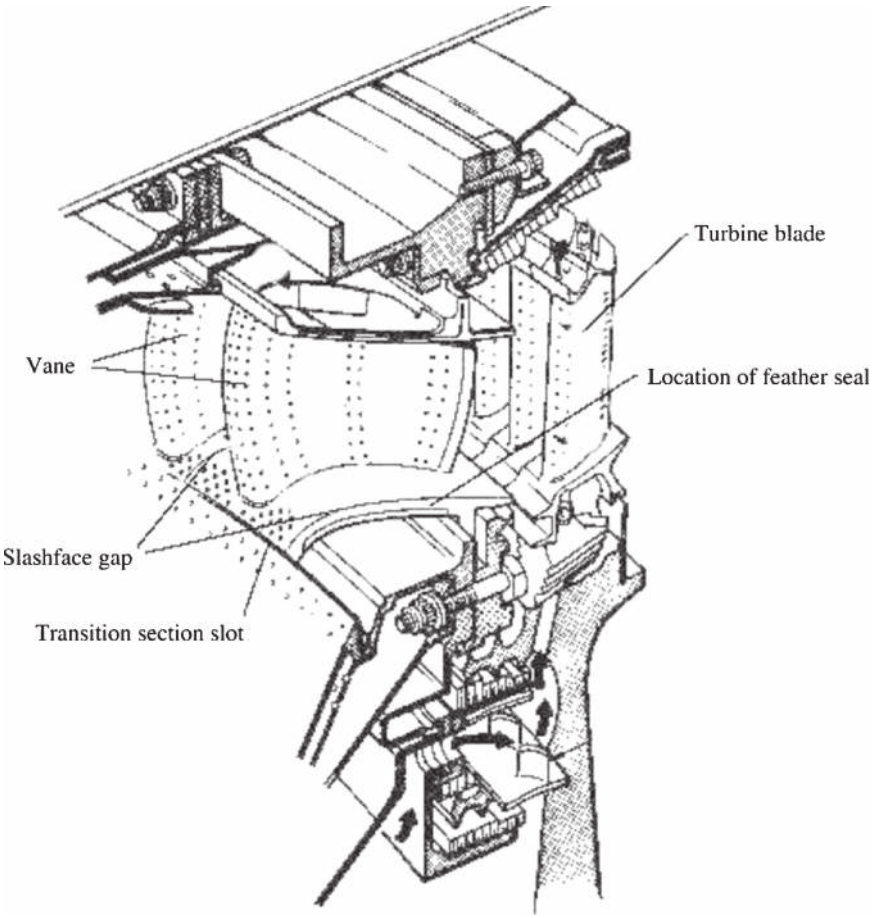

Figure 3: First stage vane and rotor section showing the transition section to vane slot as well as the slashface or gutter gap (from Cumpsty [4]).

thermal control mentioned above are applied to this section: film cooling, impingement cooling, internal convection, pin fins augmentation, and trailing edge and tip cooling. The airfoil surfaces and the endwalls are actively cooled by an appropriate choice of these techniques. Because of thermal expansion of components, the airfoils/endwall assemblies are segmented, having one or two (doublet) airfoils per assembly. The segments are separated by a gap to allow for thermal expansion, the interface gap (also known as the slashface or gutter, see Fig. 3) is sealed by air taken from the engine cavity. This sealant or leakage air is cool and mixes with the passage flow near the endwall surface and so it has important effects on the gas path cooling. Because of mixing with passage flow, which is of high velocity in the downstream half of the passage, there may be strong aerodynamic losses associated with this leakage.

The passage flow next enters the first stage rotor. In this stage, swirl is removed from the flow, while the velocity decreases and work is extracted. This work extraction

results in a drop in stagnation temperature. Though the fluid velocity drops, the net effect of velocity change and work interaction is a drop in static temperature across the rotor passage (within the passage core flow). This stage is rotating; thus, the endwall, or platform, is moving relative to the endwall of the upstream vane row. The flow in the near-endwall region thus is skewed as it passes onto a moving platform from a stationary endwall. To accommodate the relative motion of the two rows and the thermal growth of the components, there is a gap between the vane and rotor sections (see Fig. 3). This gap is sealed with airflow from the cavity, again with effects on gas path heat transfer and aerodynamic losses. The degree of skewing mentioned above can be modified by introducing the sealant flow with pre-swirl. Because of rotation, the flow and heat transfer are affected by buoyancy forces within the centripetal force field and by Coriolis forces wherever there is a radial flow component, such as with the internal cooling channels.

As the flow proceeds through the remainder of the turbine, it passes through a series of vane and rotor components of subsequent stages. In each stage, work is extracted and the total temperature is reduced, while the loss penalty for the system due to cooling air usage continues to accumulate (the coolant air used in a downstream stage is not available to do work within an upstream stage). The reduction in stage temperature has a significant impact on the choice of materials and cooling schemes. Parts with lower external heat loads (such as the second blade) tend to require less aggressive internal cooling, resulting in reduced thermal gradients within the part material (compared to the gradients in the first stage blade). Also, there are fewer internal ribs used to divide internal cooling passages and, since they tend to remain much cooler than the external walls, they carry much of the centrifugal stress load. This reduces the significance of local surface failure modes, such as oxidation, and increases the relative importance of creep, which may be understood as a section average temperature and stress-related failure mode. The change in the life limiting failure mode and the reduced external heat loads may allow the designer to choose less exotic materials or apply less aggressive thermal control, thereby reducing the cost of the part. In the large castings found in industrial gas turbine engines, the greater cost benefit may be realized by choosing less exotic materials. In the case of the smaller castings found in aircraft engines, machining costs may dominate the part price, driving the designer to choose a less complex cooling scheme. In both cases, the thermal design techniques are those employed in the first stage, but are applied more sparingly in the downstream stages.

Other components demanding thermal design attention in the gas path are support struts and the engine propulsion nozzle (in the case of the aircraft gas turbine). Thermal loads on these components are more severe if the engine is equipped with an afterburner, a combustor in the gas path upstream of the nozzle. Our more detailed discussions to follow will be restricted to the vane and rotor stages of the turbine.

2.1 The first stage high pressure turbine vane

The combustor exit turbulence level for a low-NO_x style of combustor can be as high as 20–25% [1]. The engine manufacturer generally obtains data on the flow field for a particular combustor, as it will depend on the combustor geometry.

However, several studies existing in the open literature give an indication of the turbulence levels that may be expected at the exit of the combustor. Measurements that are frequently referred on combustor exit flow conditions are by Goldstein *et al.* [5], Moss and Oldfield [6], Goebel *et al*. [7], van Fossen and Bunker [8], and Ames *et al.* [9]. A conclusion of the Moss and Oldfield study was that turbulence level and spectra are not strongly affected by whether there is combustion or not, or by the combustion rate when there is combustion. The data of Goebel *et al*., with and without combustion, include measurements of profiles of turbulence levels and exit temperatures. They found values of around 10–12% with a small but measurable drop in turbulence intensity between the unfired case with cold inlet flow and a fired case. Their combustor was designed to create significant swirl of the mixing region flow (see Fig. 4). The drop in turbulence was more in the swirl component of turbulence than in the axial component. The turbulence components were normalized on the axial inlet velocity (no swirl component in the normalizing velocity).

The radial distribution of temperature at the combustor exit is important for the design of the turbine passage endwalls. Over recent years, redesign of the combustors to improve NO_x emission and increase average turbine inlet temperatures has led to flatter profiles and, thus, hotter fluid and higher thermal loading in the near-endwall regions of the turbine. Figure 5 shows representative temperature distributions taken from Goebel *et al.* Figure 6 taken from Povey *et al.* [10] shows the radial and circumferential temperature distributions as measured in a military engine.

Next, the flow approaching the vane section is discussed. Ames *et al.* [9] noted that vane inlet turbulence depends on the nature of the flow in the core of the combustor, including residence time (as discussed above), but it is modified by the inlet contraction ratio of the transition piece between the combustor and the turbine. The cross-sectional area of the duct decreases in the streamwise direction and, thus, the flow is accelerated. As a result of this acceleration, the turbulence of the passage flow is stretched and partially dissipated and the passage wall boundary layers, which will become the vane passage endwall boundary layers, are thinned. To accommodate thermal growth of components, the passages are assembled with gaps in the wall. These gaps are sealed against ingression of hot gases with flow from the cavity of the engine (see Fig. 3). This flow will emerge into the passage and thicken the passage wall boundary layers, as it mixes with the passage flow. In addition to the sealant flow, there may be intentional film cooling flows in the approach duct, usually just upstream of the airfoil leading edge plane, which modify the approach flow boundary layer. Factors that influence the approach flow boundary layer growth are, combustor design, leakage (or sealant) flow configurations, film cooling flows, roughness, streamwise acceleration, free-stream turbulence levels and scales, and surface streamwise curvature. Thus, each design will have different wall boundary layer characteristics. Piggush and Simon [11] simulated a low-NO_x combustor and a transition section, in their study of heat transfer in the first stage vane, then documented the flow characteristics 1.5 and 0.1 axial chord lengths upstream of the airfoil leading edge plane (before any leakage flow is introduced). They noted that the aerodynamic losses associated with the boundary layers on the walls that were to become the passage walls were less than one percent of the total aerodynamic losses encountered

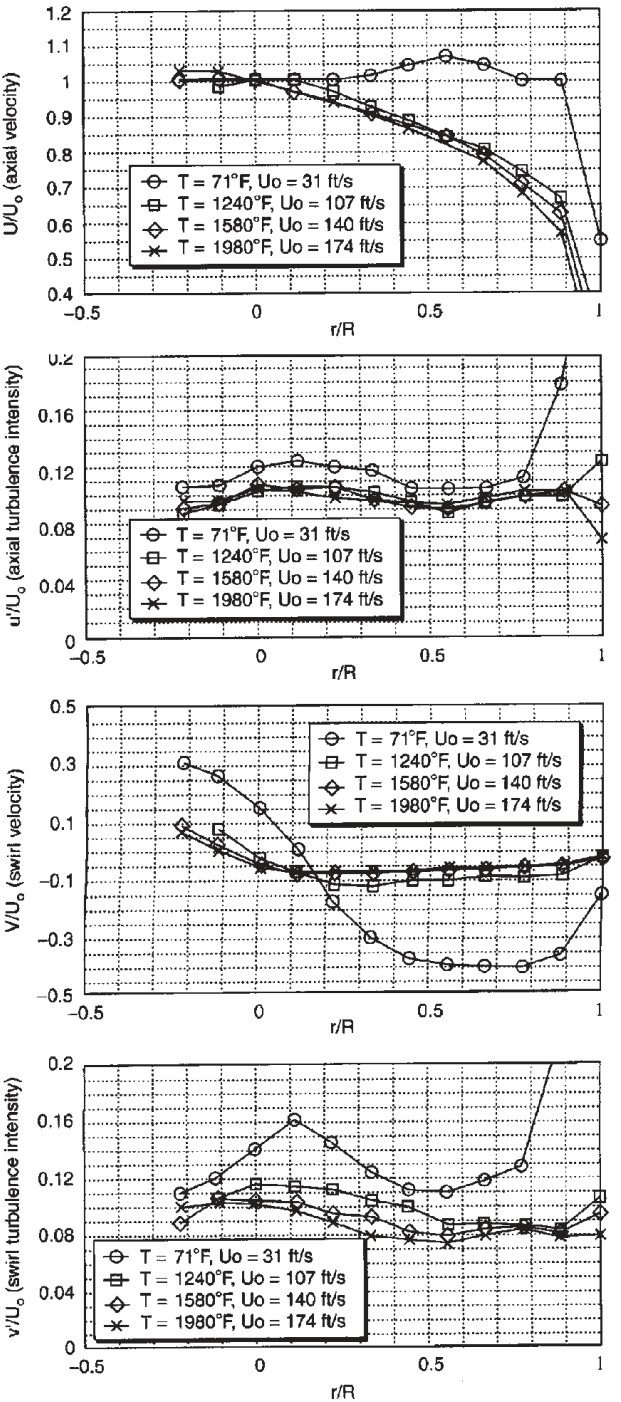

Figure 4: Effects of combustion on axial velocity, axial turbulence intensity, swirl velocity, and swirl turbulence intensity (from Goebel *et al*. [7]).

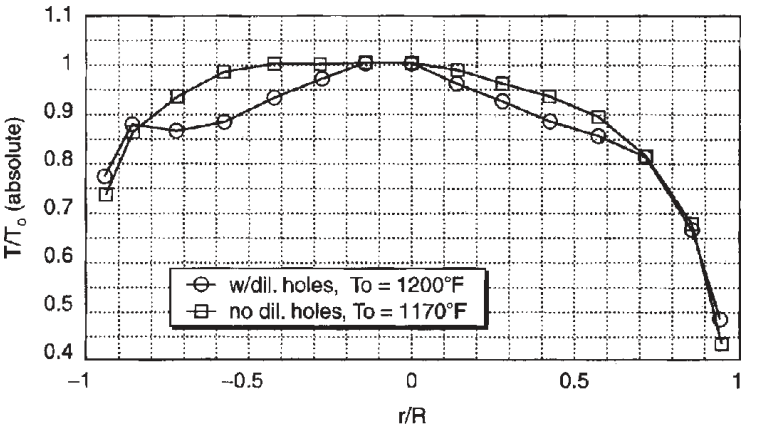

Figure 5: Effect of dilution holes on spanwise temperature distributions for similar firing temperatures (from Goebel *et al*. [7]).

within the vane row passage. Nominal turbulence intensity, the rms fluctuation of the velocity scaled on the mean velocity, in their simulation was 21% at the first measurement station and 12% at the second where the mean velocity was about 75% higher than at the first station. The integral length scale of the approach flow turbulence at the first measurement station was about 20% of the true chord length and the energy length scale [12] was about 6% of the true chord length. The momentum thickness of the boundary layer at the first measurement station was 3.24 mm [13], which is approximately 1% of the true chord length.

Cascade entrance turbulence length scales were documented for a mock combustor by Ames [14]. His geometry is similar to that used by Piggush and Simon. He used the energy length scale, Lu, for characterizing the turbulence. The energy length scale is computed from the one-dimensional (based on streamwise velocity fluctuation component only) power spectral distribution. This length scale is computed from the turbulence intensity level, u', and the turbulence dissipation, ε, as:

$$Lu = 1.5\left|u'\right|^3 / \varepsilon \tag{1}$$

where ε is computed from the inertial subrange of the power spectral density distribution. This is done by generating the spectrum, $E_1(k_1)$, and fitting the inertial subrange portion of it with the universal curve (see Fig. 7):

$$E_1\left(k_1\right) = 1.62\ \ (18/55)\varepsilon^{2/3}k_1^{-5/3} \tag{2}$$

The wave number, k_1, represents the local frequency for a given point in the 1D spectrum. Once the fit is established, select a point on the line and use its coordinates to compute ε. Ames found that this length scale is 23% of the true chord length for his mock-up combustor/airfoil study with a turbulence level of 12.9% when a short spool is used between the combustor and the airfoil row and is 30% of the true chord length and the turbulence level of 8.3% when a long spool is used. In the paper

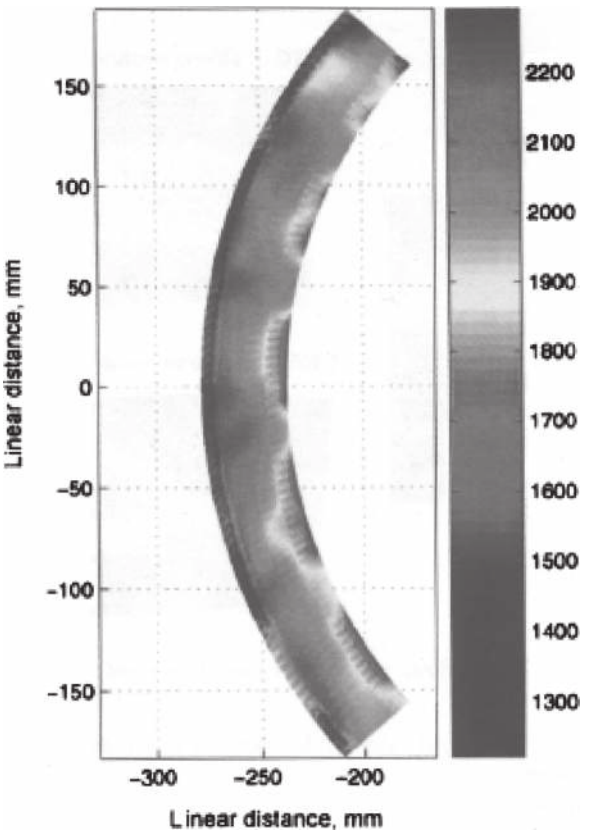

Figure 6: Measured combustor exit temperature profile – a grayscale image of a color picture. Dark regions to the right of the 1900 K contour are cooler than 1900 K and dark regions to the left are hotter than 1900 K (from Povey *et al*. [10]).

referred, Ames continues by recording the turbulence length scale effect on turbine airfoil surface heat transfer, to be discussed later in this chapter.

An example of the first stage turbine incoming flow temperature profile is provided by Povey *et al.* [10] from the data taken by Chana *et al.* [15]. Figure 8 shows a 15% variation from wall to center-span on the temperature ratio, $T/\overline{T}$ ith most of the change within 15% of the span from the wall (see "Typical engine").

3 Active cooling of the gas turbine components in the gas path

As discussed in the Section 1, stage temperature profiles of gas turbine engines often exceed the temperature capability of the turbine materials. To correct the problem, designers incorporate passages and heat transfer augmentation features on the internals of airfoil castings. When relatively cool fluid drawn from the compressor is

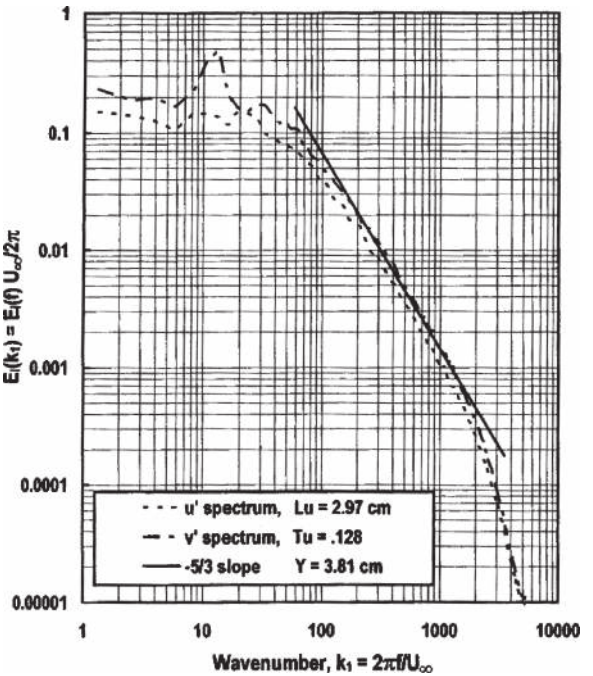

Figure 7: One-dimensional spectra of *u*' and *v*' for the combustor with a short spool showing the inertial subrange isotropy (from Ames [14]).

passed through the internal passages, the metal temperature of the airfoil can be maintained below the limits defined by material capability. The design of these internal passages has evolved over many years leading to configurations that are complex and highly effective. Some of the most popular schemes are highlighted in the following portion of the chapter.

3.1 Impingement cooling

Impingement cooling can be a very effective way to cool internal surfaces of a turbine airfoil. Properly designed impingement cooling schemes tend to have high heat transfer coefficients but also large pressure drops. As impingement cooling systems require some rather unique geometries; a feed plenum, hole plate, and an impingement target and plenum, the use of impingement cooling systems is typically confined to the first stage vane (where the high heat loads and relatively low cooling supply pressure to passage dump pressure ratio precludes the use of long-channel cooling circuits) and the leading edge and trailing edge regions of other airfoils. There are several mechanisms associated with the impinging jet that improve heat transfer. These will be discussed in the following sections.

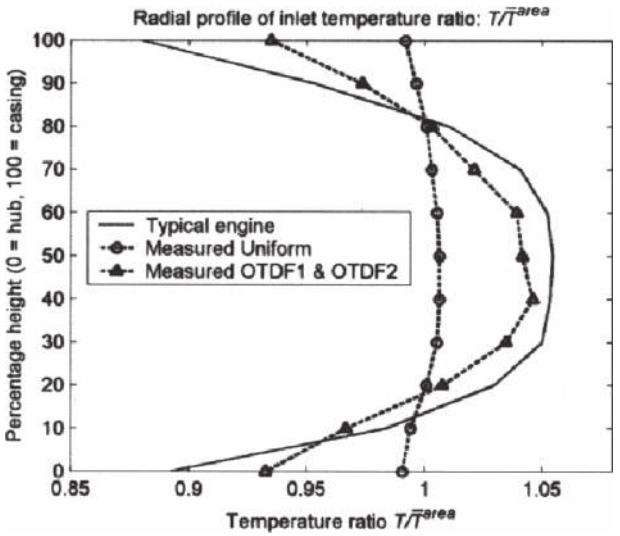

Figure 8: Circumferentially averaged temperature distributions at the turbine vane inlet. Shown is a measured profile in a real engine (typical engine), a measured profile in a simulator in which distortions due to discrete fuel and dilution air injection and endwall cooling flows are active (OTDF1 and OTDF2), and a profile measured in the simulator when the inlet temperature distortion mechanisms are not active (measured uniform).

3.1.1 Single jets

The structure of the impinging jet is of interest. A schematic of a representative geometry is shown in Fig. 9. In the simplest case, the jet flow originates in a plenum where the coolant fluid has little or no momentum. The fluid passes through a hole or slot into a lower pressure zone, driven by the pressure difference between the two plenums. As the fluid passes through the hole, it may be thought of as a slug flow with a negligibly thin boundary layer around the edge of the jet and a very flat velocity distribution across the jet core (as shown in Fig. 9). The thin boundary layers can be attributed to the rapid spatial acceleration of the flow approaching the hole exit plane. The jet has relatively high momentum as it passes into the low-pressure zone. The flow on the periphery of the jet shears on the low momentum fluid external to it, eventually leading to a breakdown of the shear layer into a train of large turbulent eddies. This causes the jet to widen and entrain external flow. The velocity profile of the jet becomes non-uniform, as shown in Fig. 9. If the jet length to diameter ratio is sufficient, the shear layer between the jet and the surrounding flow consumes the core of the jet, which leads to high levels of turbulence in the vicinity of the center of the jet. The large eddies in the shear layer also establish circulation in the low-pressure plenum, mixing that fluid. Finally, the jet impinges upon the target surface. Due to the high momentum of the jet perpendicular to the wall, the boundary layer at the impingement point is

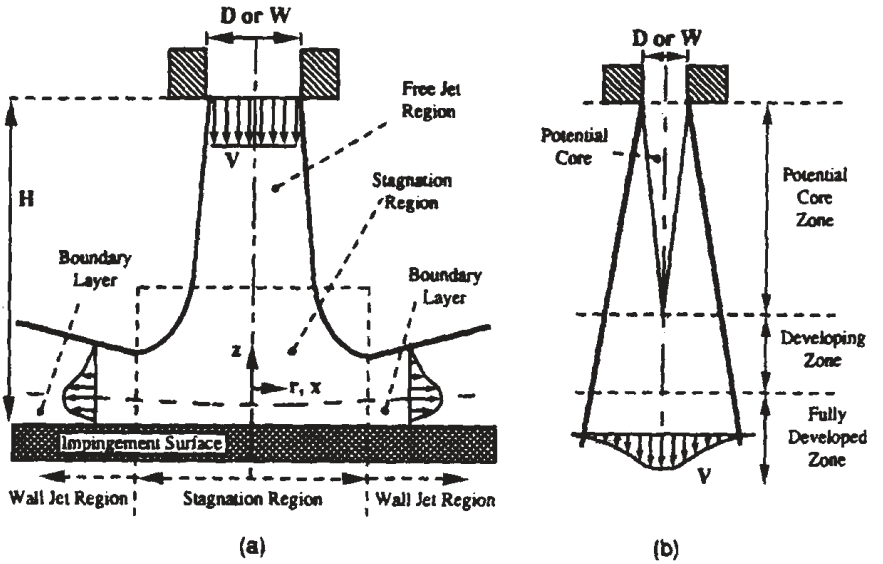

Figure 9: Different regions of an impingement jet (from Viskanta [16]).

extremely thin, while the location of this point is typically unstable. The instability is associated with the axial compressive straining of the flow as it approaches the stagnation point. As the fluid of the jet moves from the point of impact, its spatial acceleration is high, creating a thin boundary layer with a highly turbulent external flow. The net result of these processes is a high heat transfer coefficient at, and in the vicinity of, the jet impact center.

Correlations are available to describe the average heat transfer achieved with a single jet. One study is by Goldstein *et al.* [17]. In their correlations, below, the values of A, B, and C are 24, 533, and 44, respectively. The parameter R is the distance from the geometrical center of the jet, L is the distance from the orifice plate to the impingement wall, and D is the jet diameter. The correlations indicate that a maximum average heat transfer coefficient can be achieved with a distance of $L/D = 7.75$. This is sufficiently long for the non-turbulent core of the jet to be consumed, but short enough not to lose the momentum of the jet to excessive spreading.

$$\frac{\overline{Nu}}{Re^{0.76}} = \frac{A - |L/D - 7.75|}{B + C\left(R/D\right)^{1.285}} \text{ for constant surface heat flux} \tag{3}$$

$$\frac{\overline{Nu}}{Re^{0.76}} = \frac{A - |L/D - 7.75|}{B + C\left(R/D\right)^{1.394}} \text{ for constant surface temperature} \tag{4}$$

Note that there is sensitivity to the thermal boundary condition of the target plate, isothermal or of uniform heat flux. The Nusselt number of a laminar boundary

layer is known to be dependent on the thermal boundary conditions whereas a turbulent boundary layer is nearly independent of the thermal boundary conditions.

3.1.2 Impingement arrays

The single jet is of academic importance and helps introduce the reader to the general physics of the flow field. In turbine applications, impingement jets are typically arranged in two- or three-dimensional arrays. Both arrangements tend to be strongly influenced by the effect of cross flow, which develops as the spent jet air exits the stagnation zone on the target surface. Cross flow interaction with the jet causes the development of several important flow structures in addition to the jet shear layer vortex structure discussed above. The interaction of the jet fluid and the endwall boundary layer creates a counter-rotating vortex pair. The flow structure and mechanism causing the vortex pair is similar to a cylinder in cross flow and its interaction with the endwall boundary layer. The cross flow perceives the jet as an obstacle and passes around it, and a horseshoe vortex is formed. Finally, behind the jet, there exists a wake zone characterized by the presence of what Kelso *et al.* [18] term the upright vortex and also the presence of wall vortices. The vortices are shown in Fig. 10. For a more extensive treatment of the interaction of the jet and cross flow, the reader is referred to the thorough work of Kelso *et al.* [18] and also Lee *et al.* [19]

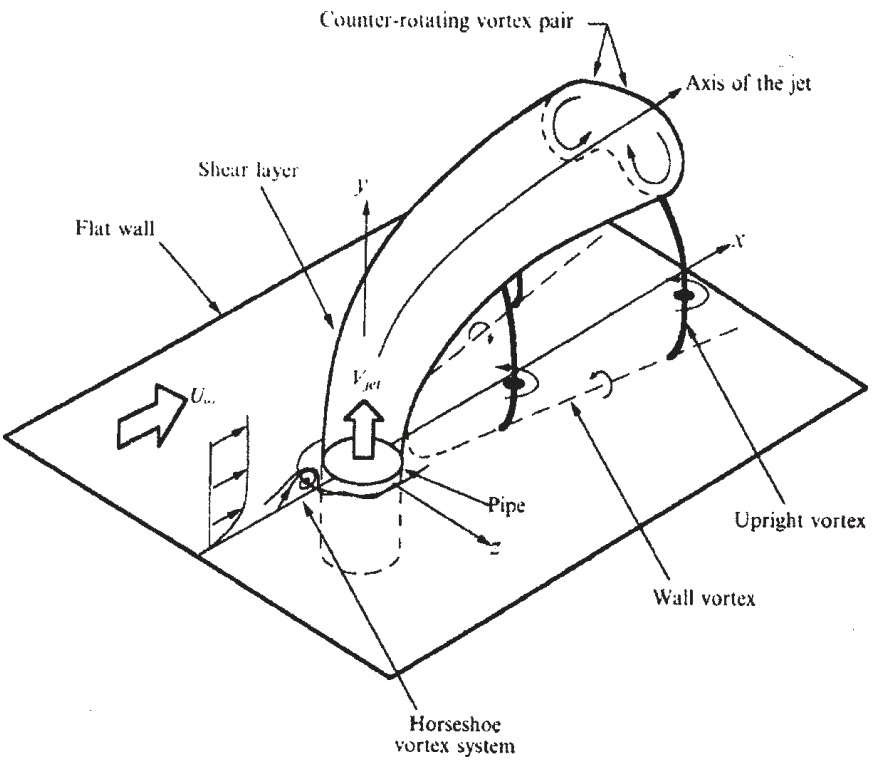

Figure 10: Vortical structures of a jet in cross flow (from Kelso *et al*. [18]).

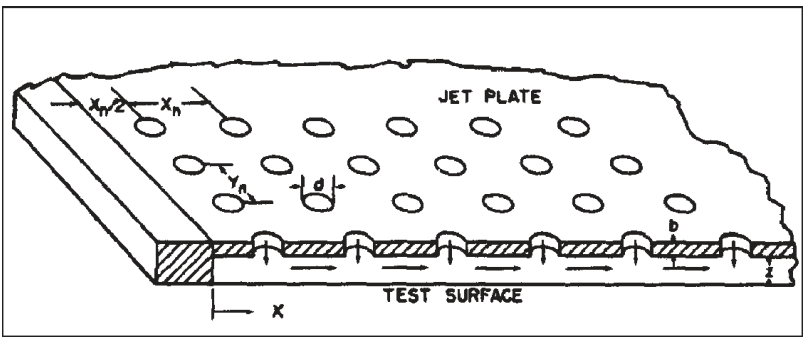

Figure 11: Sample of an impingement array showing spacing parameters (x_n, y_n, and z) (from Florschuetz *et al*. [23]).

It should be noted that in the case of impingement cooling, the jet may be interrupted by the target wall before all the flow structures outlined above have had a chance to develop fully. Such is the case when *L*/*D* is small and the laminar core of the jet extends to the impingement point. This short *L*/*D* case for a single jet was discussed by Adolfson *et al.* [20]. In this case, the impingement zone is laminar and the boundary layer flow departing from the stagnation zone transitions to turbulence as the pressure distribution dictates.

3.1.3 Jet array correlations

Some of the earliest work in this area was performed by Kercher and Tabakoff [21] who measured spatially averaged heat transfer coefficients. Their work focused on quantifying the effects of Reynolds number and jet-to-jet spacing. Several papers by Florschuetz, Metzger, and co-workers [22, 23] marked important advances in the understanding of jet array flow and heat transfer physics and also offered relatively simple correlations. Their work shows the influence of Reynolds number, hole size, jet spacing, the effects of jet-to-cross flow velocity ratio, and whether the jets are arranged in-line or are staggered. A correlation from Florschuetz *et al.* [23] is presented below.

Figure 11 shows the geometric parameters, x_n/d, y_n/d, and z/d, on which impingement heat transfer correlations have been generated (x_n, and y_n refer to the spacings between impingement holes, z refers to the impingement height, or separation between the jet hole and the impingement plate, and d is the hole diameter). The quantities G_c and G_j (Fig. 12) refer to the cross flow and jet mass fluxes, respectively. The first step in determining the heat transfer coefficient produced by the jets is to determine the ratio of the jet to cross flow mass fluxes. The idea of continuous injection of coolant as an approximation of discrete hole injection was also developed by Florschuetz *et al.* [23]. The resulting one-dimensional model may be solved analytically. The analytical solution has been validated against experimental data. Note that this model assumes that all the flow enters the system through

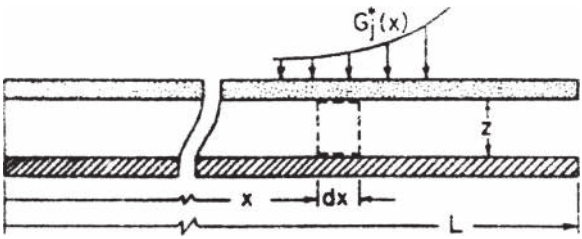

Figure 12: The continuous injection model. Here the jet flow is simulated as a continuous injection of mass along the upper plate (G_j^*) while the fluid element with dimensions of dx and z has fluid moving across its left and right faces and also into it from the jet flow injection. The discrete hole injection model shown below is an analogous configuration, which may be described by similar, discrete quantities (from Florschuetz *et al*. [23]).

the coolant jets and exits the system by moving in the direction of L. The model is given in Fig. 12.

The solution of the model is given by the following equation. This equation also requires that the discharge coefficient of the hole is known. Correlations for determining the discharge coefficient are available.

$$\frac{G_c}{G_j} = \frac{1}{\sqrt{2}C_D} \frac{\sinh \beta\left((x/x_n) - (1/2)\right)}{\cosh \beta\left(x/x_n\right)} \tag{5}$$

where

$$\beta = \frac{C_D\sqrt{2}(\pi/4)}{(y_n/d)(z/d)} \text{ and } x = x_n(i\text{–}1/2),\ i = 1, 2, 3, \ldots, N_c \tag{6}$$

The mass flux ratio will form the basis of the heat transfer coefficient calculation. The next step is to calculate the jet Reynolds number, which will be required in the calculation of a reference Nusselt number. The jet Reynolds number is defined as: $Re_j = G_j d/V_j$. This requires the calculation of the mass flux of a given jet. Based on the open area of the plate, pressure ratio across the jet, and discharge coefficient, the mass flux may be determined.

$$G_j = A_o C_D \left[2\rho\left(P_o - P\right)\right]^{1/2} \tag{7}$$

The parameter A_o, the open area ratio of the plate, is defined as

$$A_o = (\pi/4)/\left[\left(x_n/d\right)\left(y_n/d\right)\right] \tag{8}$$

The reference Nusselt number may be determined by using the following equation:

$$Nu_1 = 0.363\left(\frac{x_n}{d}\right)^{-0.554}\left(\frac{y_n}{d}\right)^{-0.422}\left(\frac{z}{d}\right)^{0.068} Re_j^{0.727} Pr^{1/3} \tag{9}$$

When the ratio of the mass of the cross flow to the mass of the jet flow is known, along with a host of geometrical parameters, a ratio of the final Nusselt number to the reference Nusselt number may be calculated from the following equation and constants.

$$\frac{Nu}{Nu_1} = 1 - C\left(\frac{x_n}{d}\right)^{n_x}\left(\frac{y_n}{d}\right)^{n_y}\left(\frac{z}{d}\right)^{n_z}\left(\frac{G_c}{G_j}\right)^{n} \tag{10}$$

	C	n_x	n_y	n_z	n
Inline	0.596	–0.103	–0.380	0.803	0.561
Staggered	1.07	–0.198	–0.406	0.788	0.660

It should also be noted that the same paper includes a more complex (and slightly more accurate) version of the correlation. For the purpose of discussion and initial design work, the equation presented here is sufficient.

3.1.4 Jet impingement arrays: areas of study

Much work on characterizing the performance of jet arrays in less general configurations is underway. A full study of this literature could not be offered in this chapter. The following is offered as a brief introduction.

Early work on characterizing heat transfer performance of impinging jets typically considered only low speed jets, which precluded the investigation of Mach number influence on heat transfer performance. Recent efforts by Park *et al.* [24] include studies with high-speed jets that show a significant dependence of heat transfer rates on Mach number (Fig. 13). The study shows increases in both local Nusselt number and line-average Nusselt number values, as shown in Fig. 14. Correlation of the Mach number data leads to a simple correction, which may be applied to the correlation of Florschuetz *et al.* [23]:

$$\overline{\overline{Nu}} / \overline{\overline{Nu}}_F = 0.58Ma^{1.35} + 1$$

A second study of interest investigates how the heat transfer coefficient can be increased by adding dimples to the target surface. This study by Kanokjaruvijit and Martinez-Botas [25] produced significant increases in the heat transfer coefficient (as much as 64%) for some jet and dimple configurations and jet-to-plate spacings. The increase in the heat transfer rate was attributed to additional vorticity created on the target surface by the dimples. Fig. 15 shows the distribution for a configuration, which produces a maximum augmentation of 51%.

3.1.5 Jet impingement on curved surfaces

Although the previous set of equations are accurate for surfaces of the airfoil that are well approximated as flat plates, they do not apply to surfaces having a significant concave curvature, as in an airfoil leading edge. A separate body of research was developed to describe this flow system and to provide correlations.

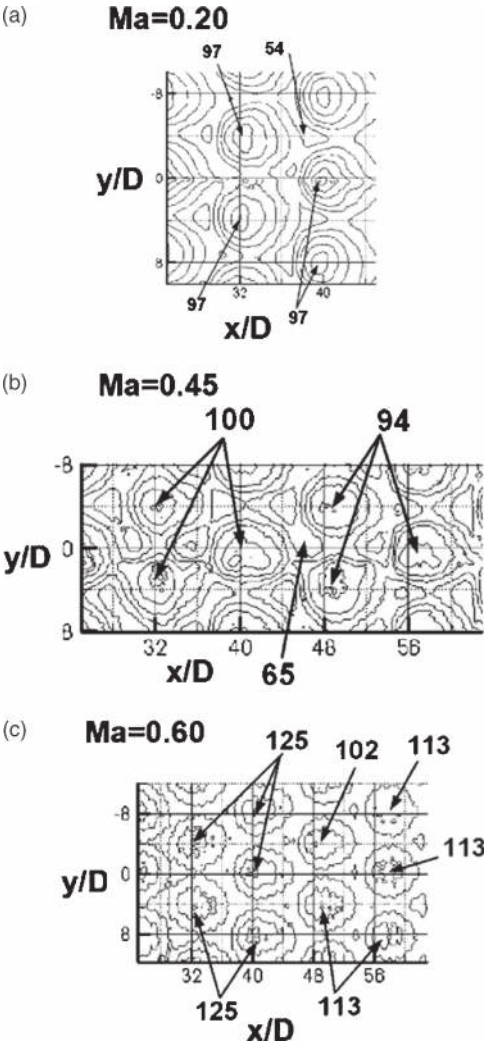

Figure 13: Spatially resolved distributions of surface Nusselt number for $Re_j = 30{,}000$ and *Ma* values of: (a) 0.20, (b) 0.45, and (c) 0.60 (from Park *et al*.[24]).

The jet flow field is similar to that already described for the flat plate jet systems. In situations which include cross flow, similar vortical structures exist, as described previously. The main geometrical differences between this system and the flat plate arrays are that the arrays typically include just a single row of jets, the target surface is curved, and the walls, which affect the spent flow departure, are positioned differently.

Chupp *et al.* [26] performed early work on the subject of leading edge jet impingement. This includes measurement and correlation of the heat transfer

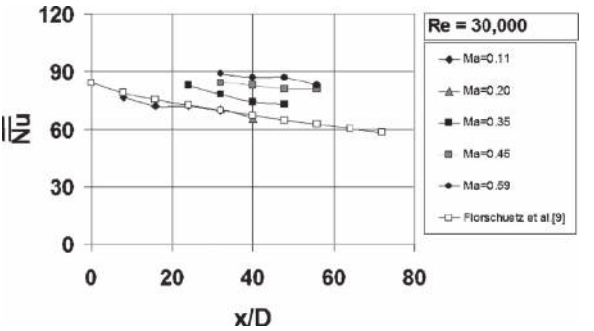

Figure 14: Comparison of spatially averaged Nusselt numbers with correlation of Florschuetz *et al.* [23]: data for Re_j = 30,000 and *Ma* values of 0.11, 0.20, 0.35, 0.45, and 0.60 (from Park *et al.*[24]).

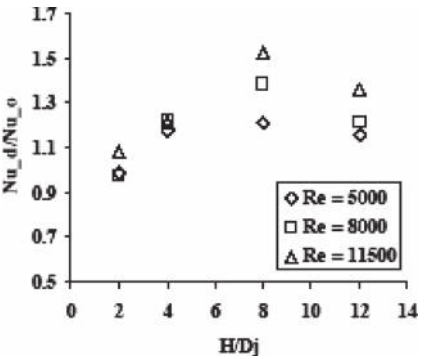

Figure 15: A comparison of normalized average Nusselt numbers at various jet-to-plate spacings, hemispherical dimples (from Kanokjaruvijit and Martinez-Botas [25]).

coefficient on the internal surface of an actual-size leading edge. The test section was configured so that the spent air exited axially (there was no cross flow). This allowed the data to be correlated on the Reynolds number and several key geometrical parameters; *d*, the diameter of the jet hole, *D*, the diameter of the target surface, *l*, the distance from the jet hole to the target surface, and *p*, the pitch of the holes. In this study, the effect of Prandtl number was considered to not be significant. The correlation for Nusselt number at the stagnation point is given by the equation below. The data also include measurements of the Nusselt numbers at locations away from the jet stagnation point allowing the average Nusselt number to be correlated as given by the second equation. The definition of the Reynolds number is given in the third equation where the diameter and mass flow rate refer to the jet.

$$Nu_{\text{stag}} = 0.44 Re^{0.7} (d/s)^{0.8} \exp\left[-0.85(l/d)(d/p)(d/D)^{0.4}\right] \tag{11}$$

$$Nu_{\text{avg}} = 0.63Re^{0.7}(d/s)^{0.5}(d/D)^{0.6}\exp\left[-1.27(l/d)(d/p)^{0.5}(d/D)^{1.2}\right] \quad (12)$$

$$Re = 4\dot{m}/\pi d\mu \quad (13)$$

Later work by Bunker and Metzger [27] and Metzger and Bunker [28] investigated similar curved leading edge geometries. The first study indicates that heat transfer rates vary with the jet Reynolds number to the approximate power of 0.6–0.7 (a result which is similar to the rates reported by Chupp *et al.* [26]). The second study reports on the impact of coolant extraction on the leading edge heat transfer coefficients. The conclusion is that jet heat transfer is primarily dependant on the total amount of jet flow with a secondary but still significant contribution due to the extraction of coolant flow through holes near the impingement site. The spent flow from the jets produces a recirculation region in the jet exhaust plenum. Drawing off spent jet air as film cooling tends to affect this recirculation. An optimum configuration of jet holes and film coolant holes can be found. The impact of the film extraction varies with the jet Reynolds number, the largest impact being produced at low jet Reynolds numbers.

3.2 Pin fin cooling

Pin fins are useful tools for enhancing heat transfer coefficients. They are often found in the trailing edge region of turbine airfoils where the high heat transfer coefficients they produce are advantageous and the relatively large pressure drops they create are acceptable. Pins can also be designed to span from one side of the channel to the other, providing a conduction path, which helps maintain the uniformity of airfoil metal temperatures. Pins also provide additional surface area, which further enhances cooling performance.

3.2.1 Pin fin flow field

The flow field around pin fins has been the subject of several studies. The results of a select group of the studies [29–31] have been used to create Fig. 16. The pin fin produces several important flow structures, including horseshoe vortex pairs and a wake region.

The horseshoe vortex pair is a flow structure which is typically formed due to a protrusion of a body from an endwall with flow across it. It is a result of a non-uniform velocity profile of incoming flow, which causes flow in some regions to stagnate at a higher pressure than flow in other regions. In Fig. 16, two horseshoe vortices are shown, the primary and secondary vortices. The wake region of the pin fin is also readily evident. This region begins after separation of the flow moving around the pin. The shear layer between the slow moving flow behind the pin fin and the fast moving flow which has moved around the pin interact causing effective mixing of the fluid behind the pin. The interface between the fast and slow moving fluid is characterized by the presence of the arch shaped vortex (similar to the upright vortex in the impingement cooling section). Additionally, the legs of the horseshoe vortices assist in the mixing the flow near the endwall. These features are visible in Fig. 17.

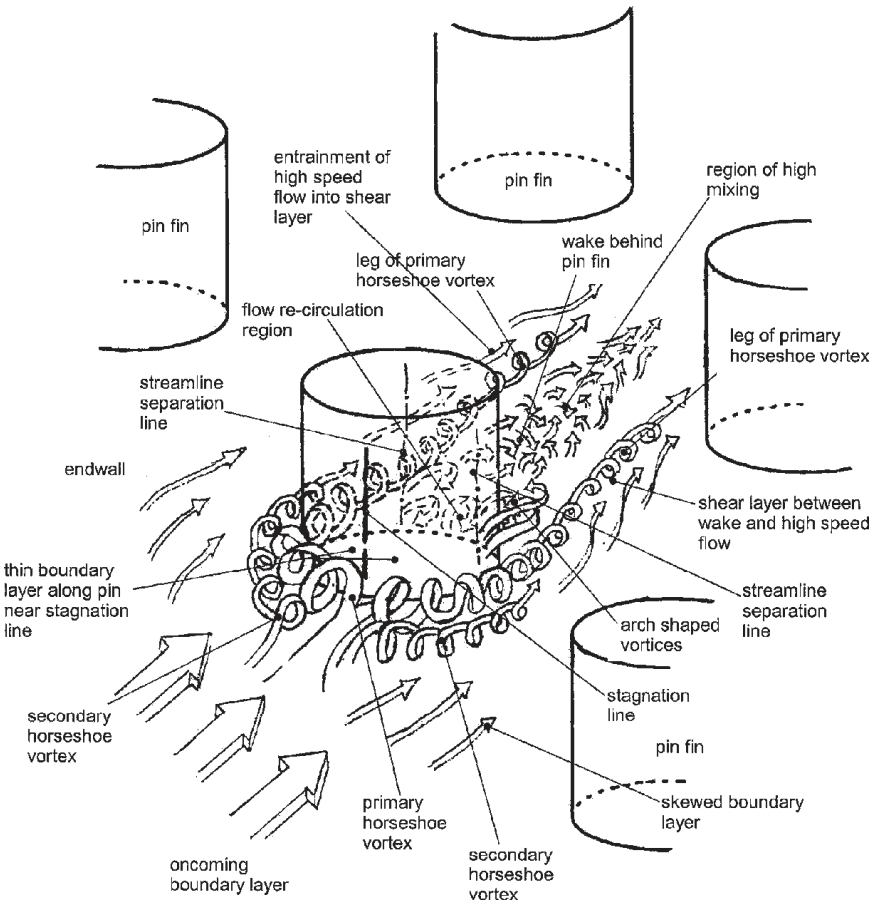

Figure 16: Flow field around pin fins within an array. The oncoming boundary layer gives rise to the primary and secondary horseshoe vortices. The pin creates a wake region with strong mixing (from Ligrani *et al*. [32])

Near the surfaces forming the pin and the endwall, the boundary layers are strongly affected by the presence of the pin. As the incoming flow stagnates on the face of the pin, the boundary layer is thin and the point of stagnation is unstable. This produces the high heat transfer coefficients well documented in other articles that show the heat transfer coefficients on cylinders in cross flow. The boundary layer builds, somewhat, as it moves around the surface of the pin until the boundary layer detaches. On the endwalls, the boundary layers skew as the flow moves around the obstruction. Behind the pin, in the wake region, the boundary layer is highly disturbed.

3.2.2 Pin fin heat transfer

As one may guess, the highest local heat transfer rates on the endwall are found near the leading edge of each pin in region influenced by the roll-up of

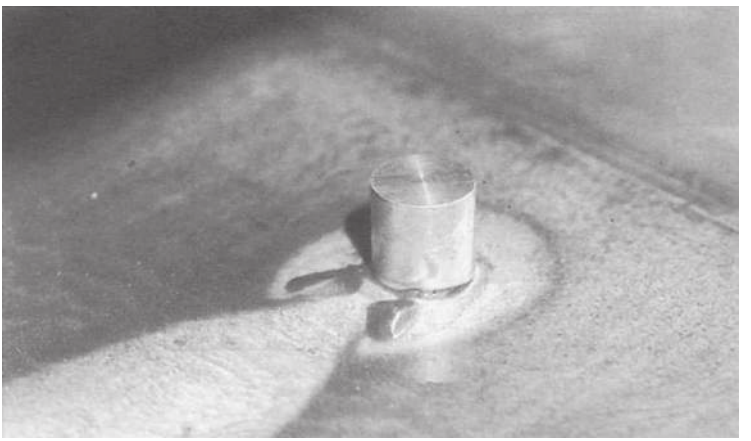

Figure 17: Oil and graphite visualization of a pin in cross flow clearly showing separation lines along the pin endwall (from Chyu and Natarajan [33]).

the horseshoe vortex. Downstream, the legs of the horseshoe vortices and the arch vortices help maintain high heat transfer rates. The work by Ligrani and Mahmood [34] clearly shows the heat transfer rates around an array of staggered pins (Fig. 18). Note that the heat transfer rates in the wake region are generally low but that the effective mixing in this region helps promote high heat transfer rates on the downstream pin. Arrays with staggered pins tend to exhibit slightly higher average heat transfer rates and a more uniform heat transfer rate distribution.

Most data on pin fin arrays are presented as row average rather than local heat transfer coefficients. This is because pin fins typically are small features and the conduction of the metal tends to smooth any metal temperature variations produced by the uneven heat transfer rates. Also, data giving the average heat transfer rate tend to be easier to collect. The average heat transfer rate at each row is a function of the Reynolds number, the configuration of the pin array (in-line or staggered), the spacing, and the size of the pins.

Row average heat transfer rates within pin arrays tend to exhibit increasing heat transfer from the first to the third or fourth row and then a slow decline in heat transfer rates (see Fig. 19). The trend is shown in the data of Metzger *et al.* [35].

The data were also correlated with the Reynolds number (based on pin diameter and the fluid velocity through the minimum flow area). For the first row of the array, the relationship is

$$Nu = 0.140 Re^{0.611} \text{ for } 10^3 < Re < 10^4 \tag{14}$$

and

$$Nu = 0.022 Re^{0.813} \text{ for } 10^4 < Re < 10^5 \tag{15}$$

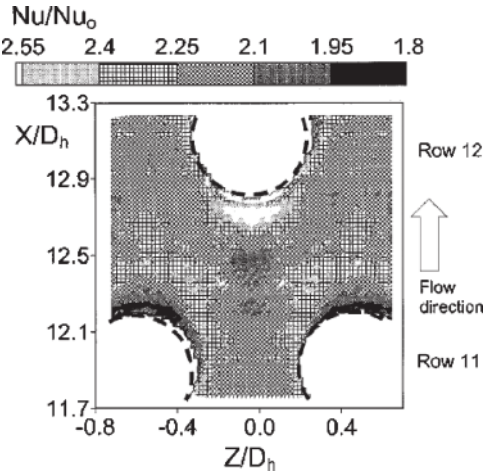

Figure 18: Local heat transfer rates around a staggered pin array, *Re* = 18,300 (from Ligrani and Mahmood [34]).

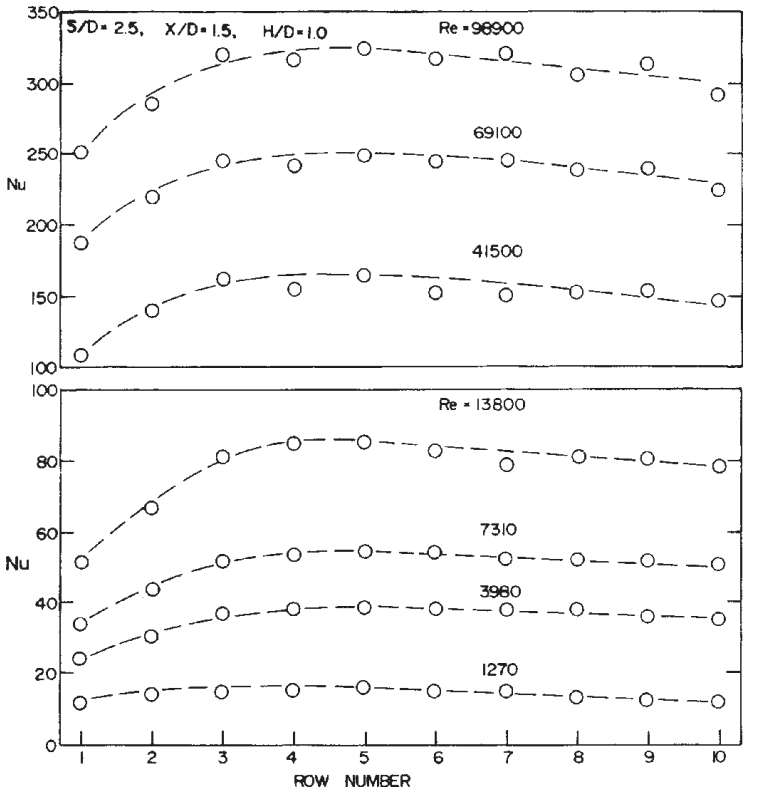

Figure 19: Nusselt number development showing the rise in heat transfer rate over the first four rows of the pin array and subsequent reduction (from Metzger *et al*. [35]).

Note that H/D of the study was unity and that the spacing between the pins across the span was $S/D = 2.5$. The average Nusselt numbers for the entire array (10 rows) were also correlated. The authors give the following relationships:

$$\overline{Nu} = 0.069\overline{Re}^{0.728} \quad \text{for } X/D = 2.5 \tag{16}$$

and

$$\overline{Nu} = 0.092\overline{Re}^{0.707} \quad \text{for } X/D = 1.5 \tag{17}$$

3.3 Channel cooling techniques

In the mid-region of turbine airfoils, some form of channel flow cooling is often employed. This cooling may be directed through a simple channel that spans the airfoil from the root to the tip (a radial flow configuration) or it may be configured in a more complex arrangement that directs the flow outward towards the tip, then inward towards the root, then repeating, through a series of channels and turns (a serpentine configuration). The number of passes that a serpentine scheme may incorporate will vary with the specific application and will depend on several factors including the external heat load, available supply pressure, internal heat transfer coefficient that can be attained, cross sectional area of the airfoil, and manufacturing considerations. Actual turbine applications typically employ three or five passes, although patents for schemes with additional passes have been filed. The channels can be either smooth or include some form of roughening elements which typically increase both the heat transfer coefficient and the pressure loss. The turns between the passages tend to exhibit complex flow fields making heat transfer coefficient and pressure loss predictions difficult.

3.3.1 Smooth channel cooling

Perhaps the simplest form of channel cooling is the smooth channel. The ability to predict heat transfer and pressure drop within the smooth channel makes it an ideal starting place when considering channel flows. Also, roughened channel heat transfer and pressure drop correlations are often presented as multipliers to smooth channel correlations.

3.3.2 Smooth channel pressure loss and heat transfer correlations

Basic correlations for smooth channel pressure drop and heat transfer have been provided by Blasius and Dittus–Boelter. The Blasius equation may be derived from the Navier–Stokes equation and solved analytically. Discussion of the solution method may be found in many heat transfer textbooks including Kays *et al.* [36]. Solution of the equation provides the following dependence for local friction factor:

$$c_f = \frac{0.664}{Re_x^{1/2}} \tag{18}$$

and mean friction factor:

$$c_{f_m} = \frac{1.328}{Re_x^{1/2}} \tag{19}$$

Used with Bernoulli's equation (the modified Bernoulli equation) the pressure drop, along a smooth channel may be determined. Many pressure loss correlations for rough channels supply factors for multiplication, which make use of smooth channel correlations as the basis.

The Dittus–Boelter equation (first proposed in 1930) has been developed to describe smooth channel heat transfer. The equation assumes fully developed flow (no entrance effects) and is often shown as $Nu = 0.023Re^{0.8}\,Pr^{n}$ where $n = 0.4$ for heating applications and $n = 0.3$ for cooling applications. The equation is often used with $n = 0.4$ as a basis for rough channel heat transfer correlations. The equation can be found in many heat transfer textbooks including Gebhart [37] and Incropera and DeWitt [38].

3.3.3 Effect of rotation on the flow field and heat transfer coefficients

Correlations for smooth channels may be used directly in the design of cooling channels on non-rotating parts. However, when the cooling channel is rotating, as in the case of a turbine blade, the smooth channel correlations must be adjusted to take into account the effects of rotation. Rotation produces a Coriolis force and, with variations in density, a buoyancy force.

The first step in understanding the heat transfer rates that will develop inside the passage is to consider the flow field. As a channel moves around an axis of rotation, fluid flowing with a radial component within the channel experiences an angular acceleration giving rise to a Coriolis force. The Coriolis force is described by the equation $\vec{F}_{Cor} = -2m\vec{\Omega} \times \vec{v}$, where m is the mass of a fluid element experiencing the force. In Fig. 20, the channels are shown rotating into the page such that the axis of rotation is to the left. The direction of the axis of the negative rotation vector($-\Omega$) is therefore to the right. By taking the cross product between the direction of negative rotation and the direction of the fluid flow, $\vec{v}$, one may find the direction of the Coriolis force. In the channel flowing toward the tip, the force is out of the page (this is represented by the arrows near the center of the channel in the cross stream depiction of the flow field, Fig. 20), while in the channel which is flowing away from the tip, the force is in the opposite direction, into the page. When viewing a cross section of the channel normal to the mean flow direction, one would find that a secondary flow circulates. Fast moving flow in the centre of the channel (unaffected by the momentum loss produced in the boundary layers near the walls of the channel) feels a large Coriolis force while a small Coriolis force is felt by the slow moving fluid in the side wall boundary layers. The pressure gradient established within the core flow pushes the low-momentum fluid in the side wall boundary layer region, causing the secondary flow field within the channel.

In channels with fluid moving away from the axis of rotation, the fluid near the leading side of the channel is stabilized by rotation, reducing turbulence, while fluid near the high pressure, trailing side is unstable (see Fig. 21). The velocity gradient

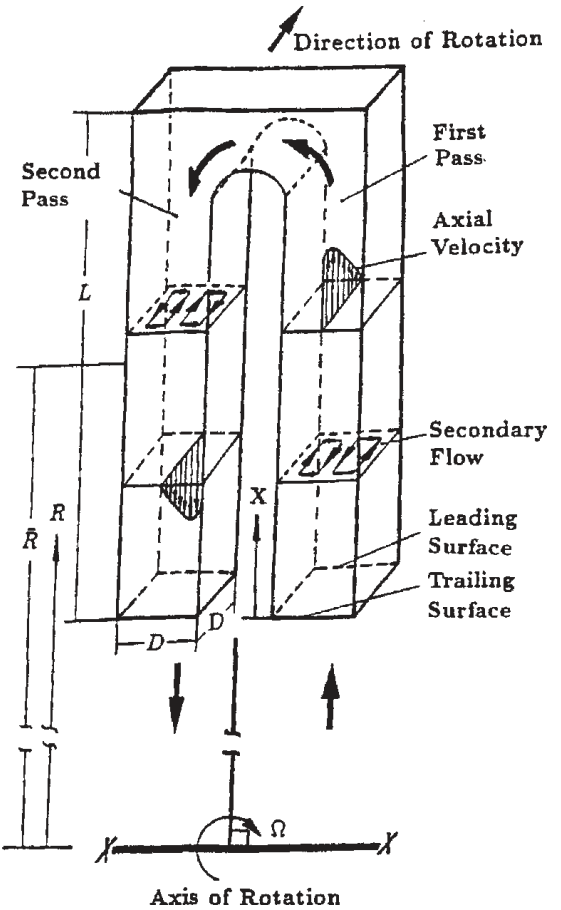

Figure 20: Depiction of the streamwise and secondary flow fields in a rotating channel.

near the unstable wall is steeper, while the velocity gradient near the stable wall is shallower. As shear stress is directly related to velocity gradient, shear stress near the unstable wall is higher, while that near the stable wall is smaller compared with those in the non-rotating channel. With these changes in turbulent mixing, we expect that heat transfer rates on the stable side will be lower than those on the unstable side.

Rotation may also induce buoyancy forces. This will affect flow if there is an imbalance of buoyancy forces, as would be the case when there is a density gradient normal to the centripetal acceleration direction. To understand the effects of buoyancy, imagine a single rotating channel with flow moving toward the tip of the channel. Let us also assume that the walls are held to the same, uniform temperature, i. e. the channel walls are isothermal. Imagine that the fluid in the core of the channel is cooler. Rotating channels impose a centripetal acceleration, $\vec{a} = -|\vec{\Omega}||\vec{\Omega}|\,\vec{R}$, on the

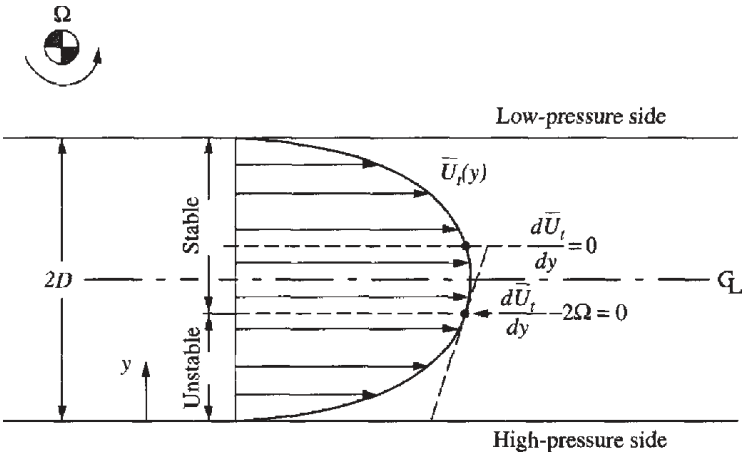

Figure 21: Regions of stability within rotating flow fields (from Lezius and Johnston [39]).

fluid (the centripetal acceleration vector points toward the axis of rotation). The parameter R is the radius from the center of rotation to the location of interest. Cooler fluid is denser and thus larger centripetal force per unit volume of fluid, $\vec{F}_{\text{cen}} = \rho\vec{a}$, is required to hold the fluid on the constant-R streamline when compared to the lower density warmer fluid near the wall. The force field causes the cooler and more dense fluid to move more quickly toward the tip of the channel while the near-wall, lower-density, fluid moves less quickly toward the tip. If the flow were to be moving radially inward, the centripetal acceleration would remain unchanged and the core flow would move toward the center of rotation less rapidly while the near-wall, warmer fluid would move more quickly. These two scenarios are shown in Fig. 22. When the Coriolis acceleration is added to the situation, the result is a velocity profile in which the wall region that is made unstable by Coriolis acceleration is peaked to a greater extent while the wall region that is stabilized by Coriolis acceleration is less peaked (these are shown in the sketches in Fig. 22). Because of the secondary flow created by Coriolis acceleration and its convection of heated and cool flows within the channel, the buoyancy and Coriolis effects cannot be treated separately.

One pioneering study on rotation effects was by Wagner *et al.* [40] This study investigates several important parameters, including the effect of density ratio ($DR = (\rho_{in} - \rho_{wall})/\rho_{in}$) and rotation number, Rot, (as presented below). The results indicate that the flow behavior described above does indeed influence the heat transfer rates.

Effects of rotation can be expressed with the following parameters:

$$\text{The Reynolds number: } Re_d = \frac{\rho d u_{\text{in}}}{\mu} \tag{21}$$

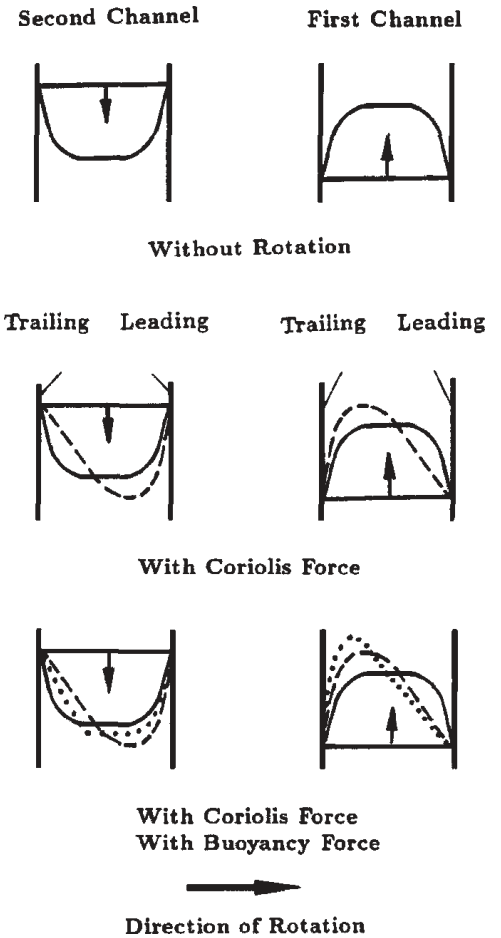

Figure 22: Effects of inertia, Coriolis, and rotational buoyancy. Note that, given the clockwise direction of rotation, the direction of the vector is out of the page (taken from Han *et al*. [1]). Solid lines, without rotation; dashed lines, with Coriolis force only; dotted line, with buoyancy and Coriolis forces.

where d is the hydraulic diameter ρ is the gas density u_{in} is the inlet gas velocity μ is the gas viscosity.

$$\text{The rotation number: } Rot = \frac{\Omega d}{u_{\text{in}}} \tag{22}$$

where Ω is the rotational frequency, and

$$\text{The buoyancy number: } Bo = \left(\frac{(T \pm T_{in})}{T} \right) Rot^2 \frac{R_m}{d} \tag{23}$$

where T is the local static temperature, T_{in} is the inlet gas temperature, R_m is the mean radius of test section.

The study by Wagner *et al.* [40] clearly shows the effect of rotation on smooth channel heat transfer (see test model, Fig. 23). In Fig. 24 (with flow moving from the axis of rotation toward the tip of the test section), the augmented heat transfer on the high pressure or trailing surface of the channel is clearly shown as augmented by the increasing rotation number. On the low pressure or leading surface, the heat transfer first decreases with increasing rotation number and then begins to increase. However, augmentation on the leading surface remains substantially lower than heat transfer augmentation on the trailing surface. As discussed above, heat transfer behavior may be attributed to the role of the Coriolis force on stabilizing and de-stabilizing the flow.

In Fig. 25 (where flow moves from the tip of the test section toward the axis of rotation), the heat transfer does not exhibit as sensitive a dependence on rotation as was seen in the flow moving toward the tip of the test section. The trends exhibited are roughly similar to those described in the previous figure.

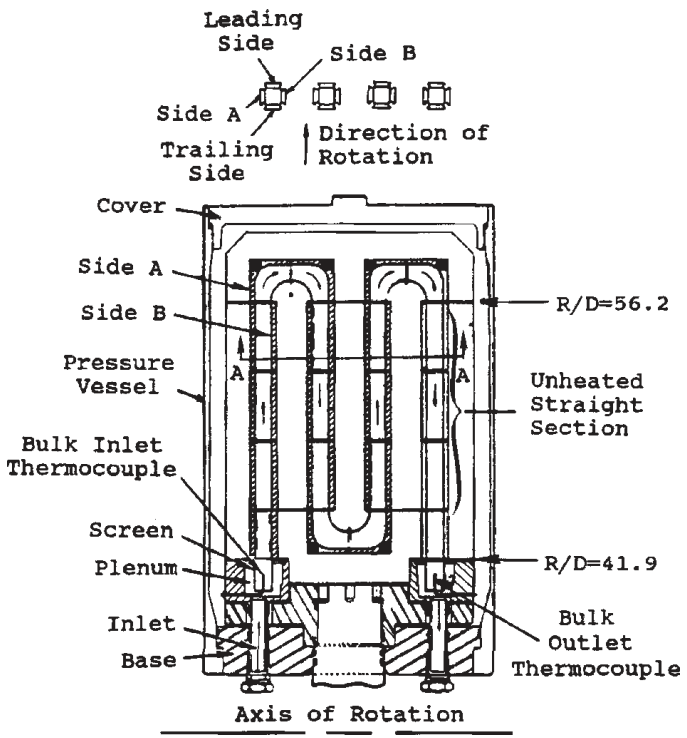

Figure 23: Serpentine coolant passage model used by Wagner *et al.* [40].

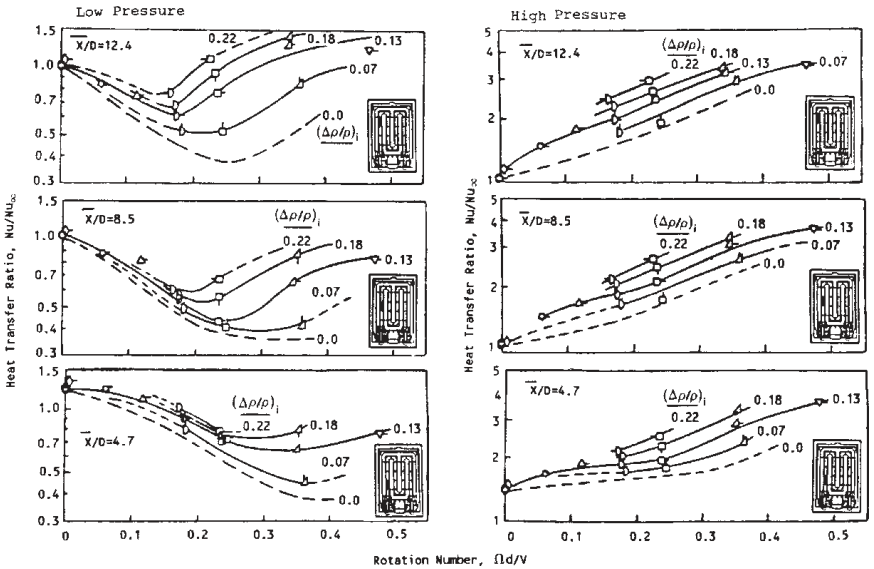

Figure 24: Effect of rotation number and density ratio on heat transfer ratio on the leading surface (low pressure) and trailing surface (high pressure) of a channel with flow moving away from the axis of rotation, Re = 25,000 (from Wagner *et al*. [40]).

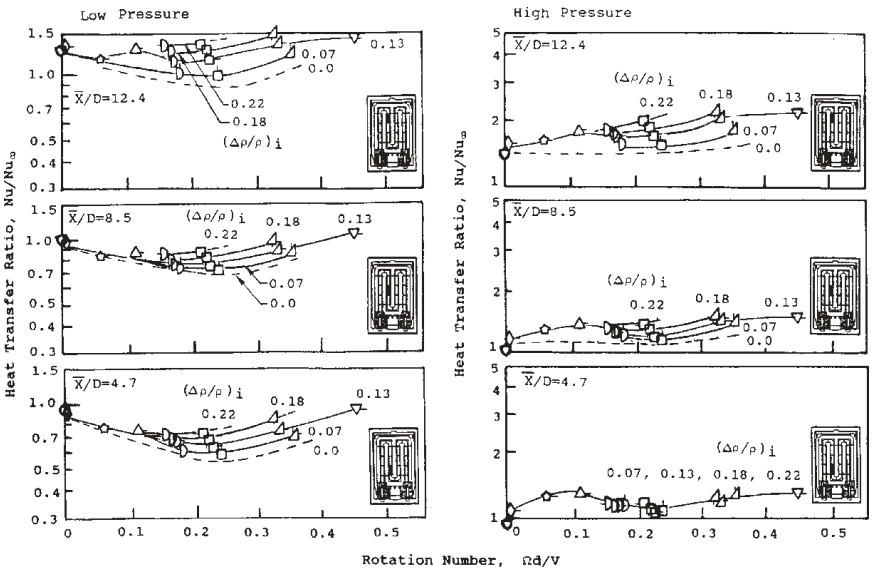

Figure 25: Effect of rotation number and density ratio on heat transfer ratio on the leading surface (low pressure) and trailing surface (high pressure) of a channel with flow moving toward the axis of rotation, Re = 25,000 (from Wagner *et al*. [40]).

3.3.4 Rough channel cooling

The heat transfer coefficients that can be obtained with smooth channels are not sufficient to transport the high heat loads of modern airfoils. To increase heat transfer coefficients, roughening is often employed on the channel walls. Perhaps the most popular method is by adding ribs.

3.3.5 Channels roughened with perpendicular ribs

Rib roughened elements can take on many forms, each producing a slightly different secondary flow structure and therefore different heat transfer coefficients and pressure drops. Casarsa and Arts [41] provide a detailed investigation of a fairly simple geometry, which is an ideal starting point for understanding the behavior of flow in a rib roughened channel. The geometry studied is a simple square channel with ribs placed on one wall and oriented perpendicular to the flow. The layout of the test section and the measurement planes can be seen in Fig. 26. The flow direction is *X*. Note that the figure is split by the plane of symmetry so that only one half of each of the ribs is shown.

The first plane of interest is the symmetry plane (see Fig. 27). This plane shows the streamwise effect of the rib. As the flow leaves the downstream edge of the rib, it detaches and a recirculation bubble is formed. At some distance downstream of the rib (in this case approximately 4.3 rib heights) the mainstream flow reattaches and the boundary layer along the wall redevelops until the presence of the next rib is felt. Here, the flow begins to rise away from the wall. A small vortex resides between the wall and the rib (shown as V_3). At the top of the rib, a small separation bubble is formed (shown as V_2).

Figure 28 shows the flow field near the smooth sidewall. Many of the same flow structures can be observed in this plane as are present at the symmetry plane. However, the nearness of the side wall causes some changes in the structure of the flow; particularly, as it approaches and moves over the rib. The momentum deficit near

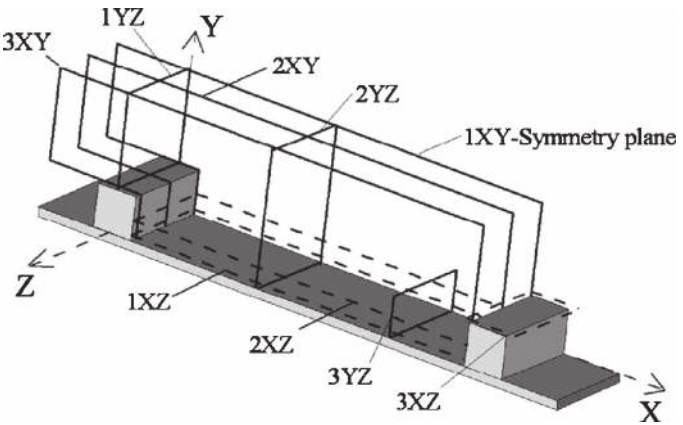

Figure 26: Layout and PIV measurements planes in Casarsa and Arts [41]).

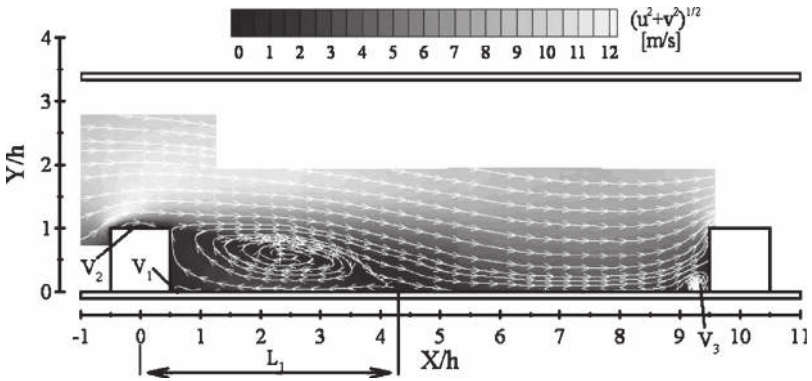

Figure 27: Time averaged velocity field in plane 1*xy* (from Casarsa and Arts [41]).

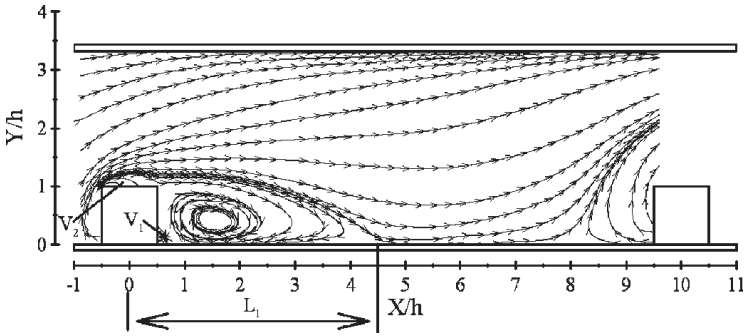

Figure 28: Stream tracer visualization of the time averaged velocity field in plane 3*xy* (from Casarsa and Arts [41]).

the side allows the vortex structure V_3 to expand, moving the separation point upstream toward the previous rib.

Figure 29 shows a plane near the rib-roughened wall. A second separation zone, S_1, is identified, located between the smooth wall and the rib. It is a result of the interaction between the low-momentum fluid near the smooth side wall, the rib boundary layers, and the recirculating flow in the separation bubble.

The final planes of interest are shown in Fig. 30. They cut across the channel and clearly show two recirculating structures, which reside at the top of the channel. They are initially created by the rib, which forces the flow upward. They intensify as the flow develops further through the passage. Away from the rib (as shown in Fig. 30, plane 2*yz*) the structures move toward the smooth walls as the channel expands downstream of a rib.

3.3.6 Effect of rib spacing and height

Typically, correlations for heat transfer in rib-roughened channels are dependent on rib spacing and rib height. Closer rib spacing tends to increase heat transfer

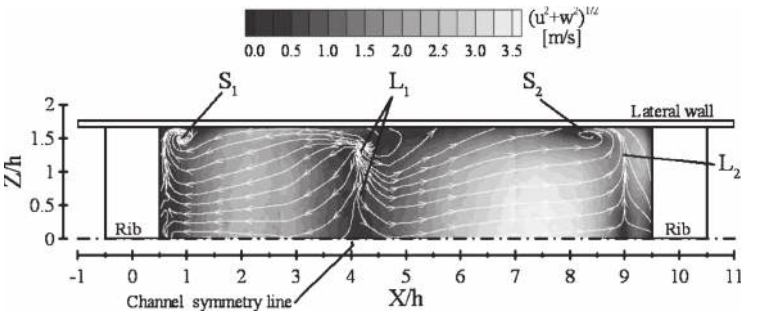

Figure 29: Time average velocity field in plane 1*xz* (from Casarsa and Arts [41]).

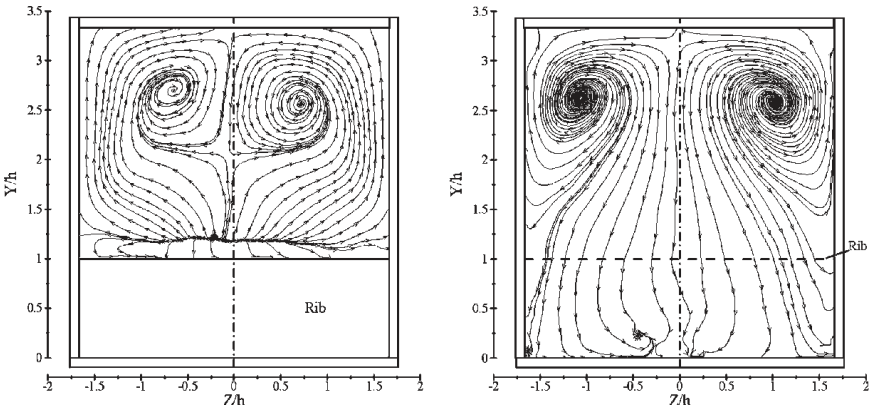

Figure 30: Time averaged flow field of plane 1*yz* (left) and 2*yz* (right) (from Casarsa and Arts [41]).

coefficients until the spacing of the ribs becomes so close that the separation zone behind a rib is not able to reattach before the next rib. At this point, correlations tend to break down and the rib roughening is no longer effective. This is often expressed as the ratio of rib height to pitch, ε/P. The height of the rib is also important and is often expressed as the ratio of height over channel hydraulic diameter, ε/D_h. Higher ribs typically yield increased average heat transfer rates. Ribs that are too low to reach above the boundary layer do less to augment heat transfer. On the other hand, ribs that are quite high may overly disturb the flow field, behaving more like baffles than roughening elements.

3.3.7 Channels roughened with skewed ribs

Channels roughened with skewed ribs exhibit some of the same flow field characteristics as the channels with perpendicular ribs. Flow tends to accelerate over the ribs, detach, and reattach at some point downstream of the rib. However, skewed ribs tend to be more effective at inducing secondary flows, which act to mix the coolant fluid, thereby increasing the effective heat transfer rates.

Kiml *et al.* [42] performed flow visualization with a water tunnel to explore the secondary flows created by skewed ribs. A sketch of the flow field with skewed ribs is shown in Fig. 31. The separation and reattachment zones are readily visible in the figure. Several additional flow structures highlighted in the schematic require explanation. The skew of the ribs produces a secondary flow near the wall which has the roughness elements (in this figure, the roughness elements are located on the left and right walls, though only the right wall is shown). This secondary flow causes the fluid near the roughened wall to flow from the bottom wall toward the top wall. The flow near the center of the passage moves in the opposite direction, from the top wall toward the bottom wall. This secondary flow pattern is shown projected toward the left hand side of the schematic. With this flow, a particle within the fluid may be expected to follow the course shown by the path lines. Note that the secondary flows in this configuration very effectively mix the coolant, circulating it from the center to the walls of the channel and also from the bottom wall to the top wall.

3.3.8 Channels roughened with ribs, heat transfer correlations

Many studies explore the heat transfer coefficients that may be obtained with rib augmentation. A review of all these studies is well beyond the scope of this chapter; therefore, only a select few are included. A more complete treatment may be found in Han *et al.* [1].

The amount of heat transfer augmentation a given configuration will produce depends on several parameters including the Reynolds number, the height and spacing of the ribs, the aspect ratio of the channel, and the angle of the ribs. The study of Fu *et al.* [43] clearly shows the effect of Reynolds number on heat transfer augmentation for both 90° ribs and 45° ribs on both the leading and trailing walls of the channel. Note the higher heat transfer coefficients observed on the trailing side of the channel. This is due to the destabilization of the trailing side boundary layer as discussed above. It can also be seen that augmentation rates on the trailing

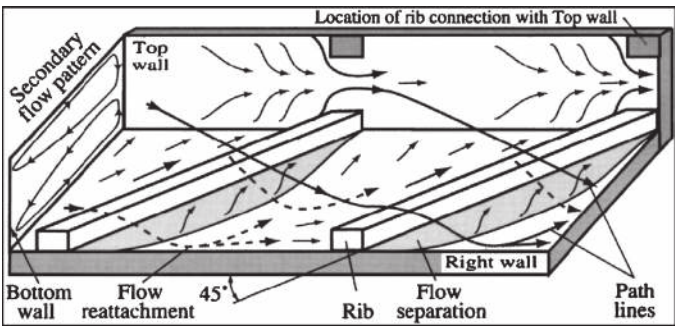

Figure 31: Flow field with skewed ribs, according to Kiml *et al.*[42]. Flow within the wall boundary moves from the upstream portion of the rib toward the downstream portion of the rib. Flow within the center of the channel moves in the other direction.

Table 1: Passage-mean Nusselt numbers and friction coefficients showing several rib configurations and a smooth channel values (from Kiml *et al.*[42]).

Rib pattern	Nu_{mp}/Nu_{mp0}	C_f/C_{f0}
Smooth	1.00	1.00
90°	2.34	15.45
75°	2.49	15.97
60°	2.67	16.24
45°	2.60	16.72

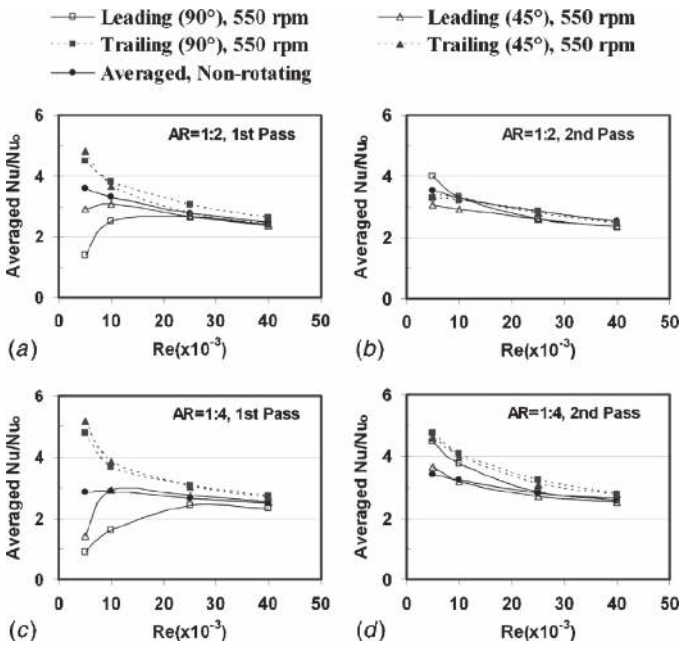

Figure 32: Average Nusselt number ratio for both rotating and nonrotating cases (from Fu *et al.* [43]).

wall tend to increase as the Reynolds number decreases. This is because the mixing and boundary layer disturbance caused by the ribs tend to be relatively more significant at low Reynolds number.

The study of Kiml *et al.*[42] provides a handy comparison of different rib orientations at constant Reynolds number and rib spacings and heights (see Table 1). It is clear that augmentation features do increase average channel heat transfer but also have a very significant pressure loss penalty. The 90° ribs are also clearly inferior to the 60° ribs, which produce the most significant heat transfer augmentation with a reasonable pressure loss.

Heat transfer over the surface of a channel is highly non-uniform, as can be seen in Fig. 33. Heat transfer rates on the channel surface near the upstream portion of

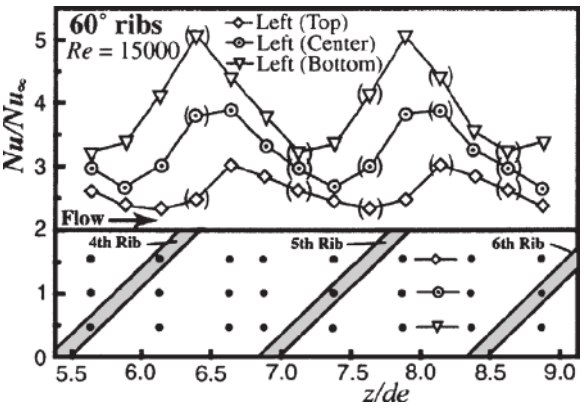

Figure 33: Local Nusselt number distribution (from Kiml *et al*. [42]).

the rib are more uniform, but are also less than the heat transfer rates on the channel surface near the downstream portion of the rib. The peaks are associated with the secondary flow along the channel wall, created in the channel by the ribs.

3.3.9 Channels roughened with V- and W-shaped ribs

As discussed above, one of the mechanisms that cause angled ribs to enhance heat transfer is the secondary flow system that they induce. The flow tends to move diagonally with the rib and then circulates back though the center of the channel. This causes one side of the channel to exhibit different heat transfer rates than the other. To reduce this difference, the ribs can be configured in a V shape. Rather than generate just two vortices, this configuration generates four vortices (see Fig. 34 which indicates the secondary flows developed by each rib configuration). The secondary flow then impacts the sides of the channel in a more uniform manner, providing a more uniform distribution of heat transfer coefficients. In the case of the W-shaped rib, the same concept is taken one step further. This configuration has a secondary flow dominated by eight individual vortices. Additionally ribs may be broken, forming discrete rather than continuous ribs.

With the V- or W-shaped ribs, the uniformity of the local heat transfer coefficients are improved over other rib configurations and average heat transfer augmentation of the V- and W-shaped ribs is slightly improved over that which can be obtained with angled ribs (see Fig. 35); however, this comes with an increased pressure penalty (Fig. 36) Similarly, the discrete configurations also tend to slightly outperform continuous ribs with an additional pressure loss. Due to the similarity in the performance (Fig. 37) of the rib configurations, the choice is not clear-cut and typically varies with the application. For instance, in some cases, the non-uniformity of the heat transfer coefficients obtained with angled ribs may be exploited to address a complementary non-uniformity in the external heat transfer rate while in other cases, the designer may find that the V-shaped configuration best matches external heat loads. The reader is referred to Ligrani *et al*. [32] for a handy comparison of the performances of different rib cooling configurations.

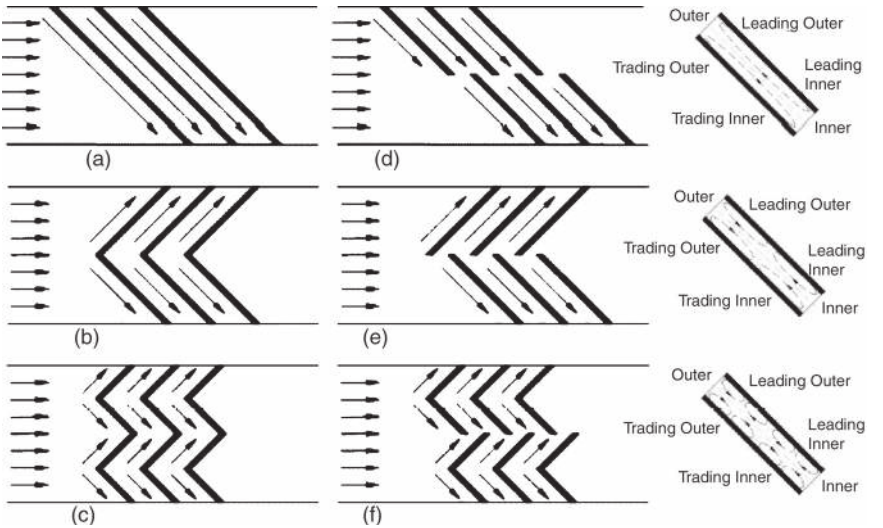

Figure 34: Secondary flows induced by different rib configurations (from Wright *et al*. [44]): (a) angled ribs; (b) V-shaped ribs; (c) W-shaped ribs; (d) discrete angled ribs; (e) discrete V-shaped ribs; (f) discrete W-shaped ribs.

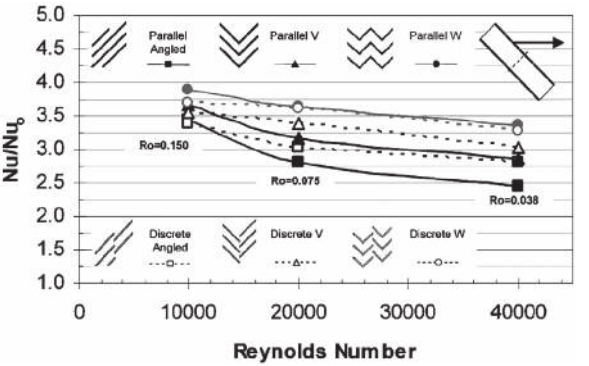

Figure 35: Channel average Nusselt number for several rib configurations in rotating channels (from Wright *et al*.[44]).

3.3.10 Dimpling

Dimpling is also an effective method of augmenting heat transfer rates, particularly in situations where only moderate increases in heat transfer rates are needed and very little pressure loss can be tolerated.

The flow field produced by the dimple is of particular interest as it is quite different from flows induced by other methods of augmentation. It is highly non-steady and is characterized by periodic shedding of vortices and fluid reattachment. As shown in Fig. 38, flow separates from the edge of the dimple forming a recirculation

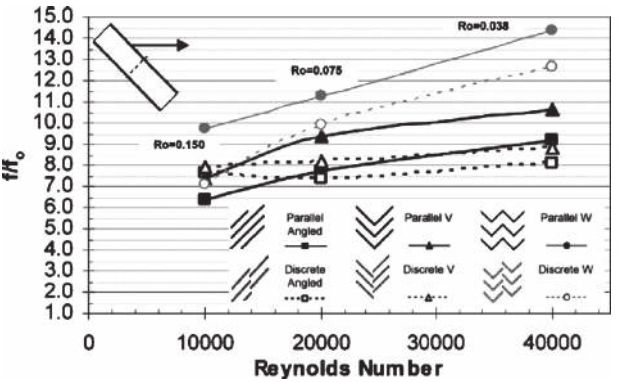

Figure 36: Average friction factor ratios for several rib configurations in rotating channels (from Wright *et al*.[44]).

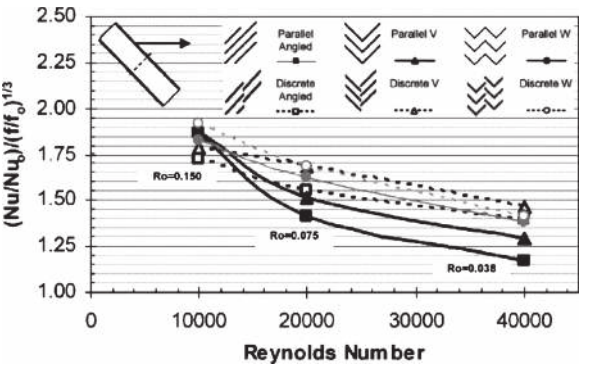

Figure 37: Thermal performance of several rib configurations in a rotating channel (from Wright *et al*.[44]).

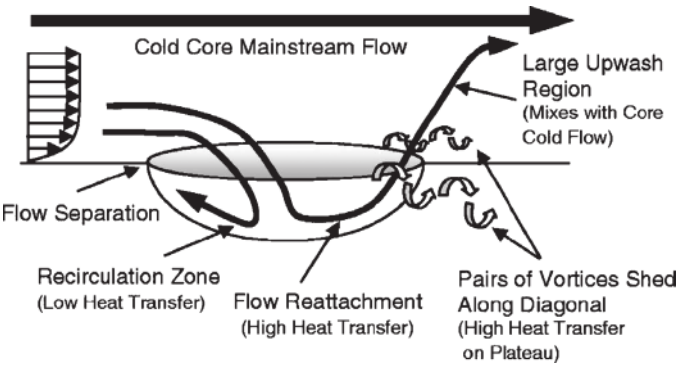

Figure 38: Secondary flow structure near a dimple (from Griffith *et al*.[45]).

zone and a reattachment point. As indicated by Ligrani *et al.* [32], the large upwash region manifests itself in a strong counter-rotating vortex pair that is intermittently ejected from the dimple. The dimple array behaves co-dependently; ejection from one dimple tends to prompt ejection events from neighboring dimples. Along the sides of the vortex pair fluid is moved downward toward the wall. Along with an ejection event, fluid rushes back into the dimple cavity causing thin boundary layers. Also, along the sides, multiple smaller vortices travel away from the downstream edge of the dimple. These secondary vortices tend to be steadier then the primary vortices.

Heat transfer augmentation produced by the dimple array is the result of both the reattachment of flow inside the dimple and shedding of vortices over the edge of the dimple. The reattachment causes the thin boundary layers typically associated with high heat transfer rates. The other dominate flow structure, namely the large counter rotating vortex which is periodically ejected from the dimple, effectively mixes boundary layer flow with the core and drives smaller vortices which enhance heat transfer along the area between neighboring dimples. Local heat transfer data are presented in Figs. 39 and 40. Note the zone of low heat transfer corresponding to the recirculation zone behind the reattachment point.

Although the heat transfer increases that can be obtained with dimples are somewhat less than what may be obtained with other augmentation features, the pressure drop associated with dimples is also less. Dimples have been shown to be one of the more efficient means of heat transfer augmentation. Dimples also produce relatively consistent local Nusselt number augmentation (see Fig. 41); an improvement over that achieved with cooling schemes utilizing rib turbulators which tend to exhibit a fairly large amount of spatial variation.

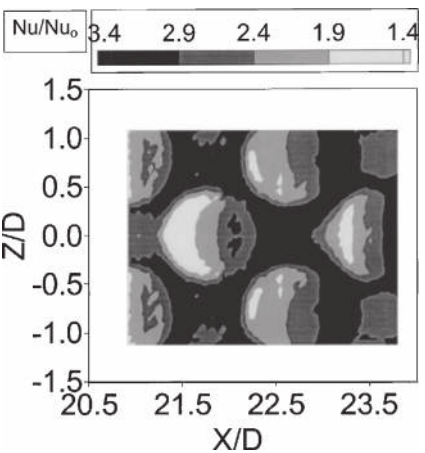

Figure 39: Local heat transfer coefficients with dimples on one channel surface, Re_H = 17,200 (from Burgess *et al.*[46]).

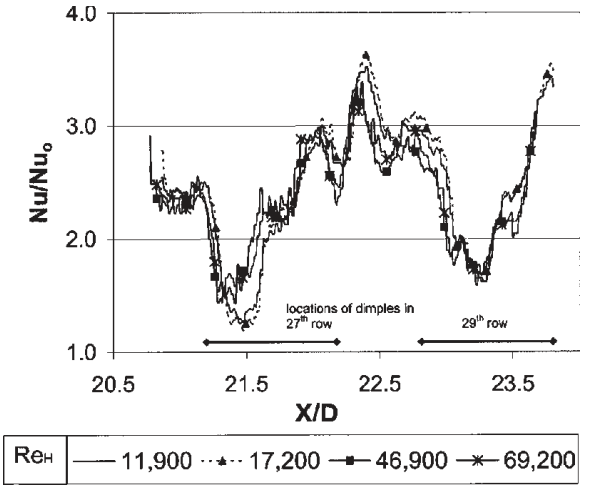

Figure 40: Local channel Nusselt numbers on a dimpled surface (from Burgess *et al*. [46]).

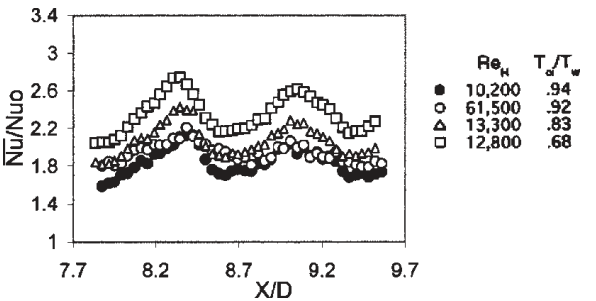

Figure 41: Spanwise average Nusselt number augmentation (from Mahmood *et al*. [47]).

3.4 External heat transfer

External heat transfer applies to surfaces adjacent to the passage flow, whether they are the airfoil external surfaces or the passage walls (endwalls or platforms). As noted, the airfoil resides in a flow of which the temperature exceeds the maximum materials temperature for a suitable design; thus, the surfaces adjacent to the passage flow must be aggressively cooled. This can be by conduction to the internal surfaces, which are cooled by the means discussed above, or by film cooling, which will be discussed in later sections. The first step in the design process is to describe the boundary conditions. The entry flow conditions to the first stage of the turbine have been discussed. The maximum surface temperature limits that the design must meet are determined by materials limitations, such as yield,

oxidation, creep, and thermal mechanical fatigue (TMF). Establishing these limits requires empirical materials data and is, therefore, outside of the scope of this chapter. As mentioned, design for external thermal control must be done in conjunction with the internal cooling design as air from the internal cooling operations is used for film cooling and the external heat load affects the coolant heat up. Thus, the coolant temperature and pressure available for film cooling are determined by the internal cooling design.

3.4.1 Airfoil external heat transfer

Important boundary conditions to the airfoil thermal design are the material temperature limits and the approach flow radial and circumferential distributions of gas temperature and flow: velocity, turbulence levels, and turbulence spectra or representative turbulence length scales computed from the spectra. The first is beyond the scope of this section; the remaining boundary conditions have been discussed. With these conditions understood, one is ready to begin the analysis.

3.4.1.1 Basic analysis An understanding of external heat transfer coefficients may be gained by beginning with a highly simplified approach. This allows becoming oriented to the relevant parameters and establishing some approximate values. To have suitable design values, more sophisticated analyses are needed.

A simple first approach is to assume that the heat transfer and flow are steady and that the geometry of the airfoil may be approximated by simple geometries: (1) the leading edge as a cylinder in cross flow, (2) the pressure side as a flat plate surface, and (3) the suction side as a flat plate. Complex regions such as the blade tip, trailing edge, or airfoil–endwall junction cannot even crudely be modeled so simply. Equations correlating the heat transfer coefficient for these simple cylinder or flat plate geometries may be found in most heat transfer textbooks. For example, a correlation of heat transfer data for a cylinder in cross flow is available in the text by Kreith and Bohn [48]:

$$\frac{h_{c\theta} D_o}{k_f} = 1.14\left(\frac{V_\infty D_o}{\nu_f}\right)^{1/2} Pr_f^{0.4}\left[1-\left(\frac{\theta}{90}\right)^3\right] \tag{24}$$

for $0 < \theta < 80^\circ$, assuming laminar flow and a low level of approach flow turbulence intensity. The parameters are: $h_c\theta$, the convective heat transfer coefficient, variable with; D_0, the cylinder diameter; k, Pr, and v, the fluid thermal conductivity, Prandtl number, and kinematic viscosity based upon the fluid film temperature; V_∞, the approach flow velocity; and θ, the position around the cylinder, where the 0° point is the stagnation line. Other than missing the effects of approach flow turbulence intensity, this will give a rather good estimate of the turbine leading edge heat transfer coefficient. Now look at computing the downstream flow. If the leading edge diameter Reynolds number is below approximately 100,000, one might expect the boundary layer to be laminar at $\theta = 80^\circ$, if above this value, a turbulent boundary layer may be assumed. This transition Reynolds number is based upon a low disturbance level external flow.

Over the region were laminar flow may be assumed, the flat plate heat transfer coefficients may be roughly calculated from a correlation of results of an analysis, as reported by, for instance, Incropera and DeWitt [49]:

$$Nu_x = \frac{h_{cx}x}{k_f} = 0.332 Re_x^{1/2} Pr^{1/3} \tag{25}$$

assuming $0.6 < Pr < 50$ and a low level of external disturbance. Choosing the origin of x as the location $\theta = 80^\circ$ on the leading edge would give conservatively high values of heat transfer coefficient. Since this correlation gives infinite values of heat transfer coefficient at the origin, there must be some fairing with the upstream leading edge heat transfer coefficient distribution at that point.

Where the flow may be assumed to be turbulent, the Chilton–Colburn analogy can be applied to compute the heat transfer coefficient. The results of this application of the analogy can be found in Incropera and DeWitt [49]:

$$St = \frac{h_c}{\rho c_p V_\infty} = 0.0296 Re_{x,\text{turb}}^{-1/5} Pr^{-2/3} \tag{26}$$

assuming a low level of freestream turbulence intensity. The origin for x may be the $\theta = 80^\circ$ location on the leading edge if the diameter Reynolds number exceeds 100,000. Otherwise, the location of transition to turbulence of the above laminar boundary layer would be a suitable choice, if it were known. A value of $Re_{x,\text{trans}} = 5 \times 10^5$ is often used as the transition Reynolds number, but the transition location is highly variable with streamwise pressure gradient, surface curvature, surface roughness, and external flow disturbance level, all of which are present and strong in turbine external surface flow analyses. Prediction of flow transition on turbine surfaces remains a major unsolved problem of turbine flow and heat transfer analysis. Nevertheless, models exist and one will be discussed below. Often, the first row of film cooling holes beyond the leading edge region can be counted upon to trip transition to turbulence on the suction surface. Thus, the origin for x,turb may be the streamwise location of that row of holes. On the pressure surface, film cooling injection may trip transition. However, if the injection is in a region of strongly accelerating flow, the boundary layer may remain laminar. Assuming that a trip to turbulence is at the film cooling hole would lead to conservatively high heat transfer coefficients. Again, since this correlation gives infinite values of heat transfer coefficient at the origin of x, turb, there must be some fairing of the heat transfer coefficient distributions at that point. However, it is known that with an abrupt transition, the heat transfer coefficient can rise rather steeply, so the fairing could be applied over a short streamwise distance. The above equations may be used together to see the relevant parameters and give a very crude approximation to the local heat transfer coefficient distribution on an airfoil.

When tripping to turbulence by film cooling injection cannot be assumed, a transition model must be applied. One rather simple model that has been shown to apply well to airfoils [50], even when applied in a quasi-steady fashion during the passing of wakes from upstream airfoils, is the correlation of Mayle [51]. In this model, the Reynolds number based upon the momentum thickness, δ_2, and the

freestream velocity, V_∞, at the point of transition is given as a simple function of the freestream turbulence intensity, Tu, (give as a percent) as:

$$Re_{\delta_2,\text{transition}} = 400 \cdot Tu^{-5/8} \tag{27}$$

The effects of acceleration are captured in the value of the momentum thickness.

Now we introduce some modifications to the simple heat transfer models that lead to more accurate computed values of heat transfer rates.

Additional accuracy can be gained on the calculation of the heat transfer coefficient in the leading edge region of an airfoil by including the effect of approach flow turbulence. Ames *et al.* [9] noted that elevated levels of turbulence augment heat transfer in the laminar region of airfoil boundary layers, especially at the stagnation region. Turbulence levels affect suction surface heat transfer mostly by way of the influence on the transition location. Increased free-stream turbulence will move the transition onset location upstream, as the Mayle correlation shows. Increases in turbulence length scales increase pressure surface heat transfer. One correlation for the effect of turbulence on the stagnation region, given by Van Fossen *et al.* [52], is based on measurements in a flow with isotropic, grid-generated turbulence.Application of it begins with a modification of the stagnation line heat transfer coefficient:

$$Fr(0)_{\text{turbulence-enhanced}} = Fr(0)_{\text{low-turbulence}} \left(0.00851 \sqrt{Tu \cdot Re_D^{0.8} \left(\frac{\Lambda_x}{D} \right)^{-0.574}} + 1.0 \right) \tag{28}$$

where the Frossling number at the stagnation line,

$$Fr(0) = \frac{Nu_D(\theta = 0°)}{Re_D^{1/2}} = \frac{(h_{c,\theta=0°} D_o / k_f)}{(V_\infty D_o / \nu_f)^{1/2}} \tag{29}$$

of the low-turbulence flow can be taken from eqn. (25). The other parameters are: Tu = the turbulence intensity and Λ_x = the integral scale of turbulence based upon the streamwise velocity fluctuation component [53]. The paper gives a value for the coefficient of 0.00851. It was later changed to 0.00792 as explained in Giel *et al.* [54]. The integral length scale is not often known in design applications. The Van Fossen et al. correlation is based upon data in the range: $0.05 < \Lambda_x/D < 0.3$. Van Fossen and Bunker [55] measured stagnation region heat transfer on a circular leading edge residing in the exit flow of a dry, low-NO_x can combustor. The flow turbulence intensity level was 28.5% and integral length scale to leading edge diameter ratio was 0.5. These can be taken as representative of that type of combustor–turbine arrangement. Their measured stagnation line heat transfer coefficient was 14% higher than that given by the Van Fossen et al. correlation. They could not say why, but noted the high degree of swirl in this combustor as a possibility. The turbulence intensity range of the correlation is: 1.1% < Tu < 15.9%. One author notes [56] better performance of the correlation when applied with turbulence levels that are closer to the correlation range.

A correlation that includes the effects of turbulence level and scale on laminar boundary layers with a constant free-stream strain rate is given by Dullenkopf and Mayle [57]. An effective Nusselt number for the stagnation region, given in terms of effective turbulence intensity, is:

$$Nu_{\mathrm{a}} Pr^{-0.37} = 0.571 + 0.01 Tu_{\lambda} \tag{30}$$

where the effective Nusselt number is

$$Nu_{\mathrm{a}} = \frac{Nu_{\mathrm{D}}}{\sqrt{a_1 Re_D}} \tag{31}$$

the parameter a_1, the dimensionless strain rate, is 4.0 for a cylinder in cross flow. The effective turbulence intensity, Tu_{λ}, is given by

$$Tu_{\lambda} = \frac{Tu_{\mathrm{a}} \sqrt{L_{\mathrm{a}}}}{(1 + 0.004 L_{\mathrm{a}}^2)^{5/12}} \tag{32}$$

the dimensionless length scale, L_{a}, is given by

$$L_{\mathrm{a}} = \frac{\Lambda_x}{D} \sqrt{a_1 Re_D} \tag{33}$$

where Λ_x is the integral length scale based upon the streamwise velocity fluctuation component. The turbulence term is given as:

$$Tu_{\mathrm{a}} = \frac{Tu \sqrt{Re_D}}{\sqrt{a_1}} \tag{34}$$

where *Tu* is based upon the streamwise component of approach flow velocity fluctuation.

Additional accuracy on the pressure and suction surfaces where the flow is turbulent can be gained by applying the simple flat plate turbulent boundary layer equation discussed above but with multipliers that account for pressure gradients. The inputs to the development of these multipliers are taken from analysis, correlation of data, or engine experience. For instance, the effects of pressure gradient and temperature ratio for the turbulent boundary layer flow on an airfoil were correlated by Rued and Wittig [58] as a modifier to a turbulent flow flat plate correlation, which is similar to the one above:

$$St = \frac{h_{\mathrm{c}}}{\rho c_{\mathrm{p}} V_{\infty}} = 0.0295 Re_{x,\mathrm{turb}}^{-1/5} Pr^{-0.4} \left(1 - F_{\mathrm{K}} \cdot \frac{K(x)}{St}\right) \cdot F_{\mathrm{T}} \tag{35}$$

where F_{K} is 165 and F_{T} is 1.08 for a wall to freestream temperature ratio of 0.64. The acceleration parameter, $K(x)$, is defined as $(\mathrm{V}_{\infty}/\mathrm{V}_{\infty}^2)/\mathrm{d}V_{\infty}/\mathrm{d}x$. The Reynolds number captures some flow history with the definition:

$$Re_{x,\text{turb}} = \int_{x,\text{turb}}^{x} \frac{V_\infty(x)dx}{\nu_\infty(x)} \tag{36}$$

When the acceleration parameter, K, exceeds ~0.5×10^{-6}, heat transfer is reduced perceptibly, as eqn. (35) shows. When it exceeds 3.5×10^{-6}, the boundary layer appears to be entirely laminar [36].

3.4.1.2 More advanced analysis Numerical prediction of heat transfer coefficients offers the gas turbine designer the opportunity to include more effects, such as those due to acceleration, curvature, roughness, elevated turbulence intensity, and, possibly, turbulence scale. The parabolic finite volume code TEXSTAN [36], based on the SIMPLE velocity and pressure solution method [59] provides additional accuracy over the method of defining the heat transfer coefficients described above. Other computational avenues are available for modeling the heat transfer coefficient. If the flow is complex, perhaps three-dimensional, unsteady, or has regions of separation, an elliptic solver is needed. Some examples of codes frequently used for gas turbine analysis are: Fluent [60], Star-CD [61], and CFX [62]. These require the construction of an appropriate two- or three-dimensional mesh and the application of a turbulence model. Several methods of turbulence modeling are available, as outlined by Han *et al.* [1] and Lakshiminarayana [2]. They discussed the Prandtl mixing length, k–ε, k–ω, algebraic stress, Reynolds stress, and large eddy simulation (LES) turbulence models and direct Navier–Stokes simulation. The LES simulation needs a turbulence closure model for only the scales of turbulence that are smaller than the computational grid scale. Subgrid scale models are expected to be applicable over a wider array of situations than the other turbulence models listed. More recently, the v^2f [63] model has been applied successfully to turbomachinery flows. Discussions on the application of these models for the simulation of turbulent flows are available in the open literature. An excellent review of such computations and comparisons of their results to experiments is given by Dunn [64]. Dunn notes that unsteady calculations often offer improved prediction of heat transfer coefficients on airfoils that are downstream of airfoil rows, such as the first stage rotor. He cites the work of Abhari and Epstein [65], which shows that the time-average of the unsteady heat transfer predictions is significantly greater, as much as ~230% of the steady-state predictions. Unsteady computations tend to represent a significant increase in computational time and software complexity over steady computations.

3.4.1.3 Heat transfer coefficient distributions The discussion of 2D airfoil external heat transfer coefficient distributions is complete. Measurements of a representative distribution, along with a computer simulation, are given by Giel *et al.*[66] in Fig. 42 as the 50% span case. One can see high levels at the stagnation point on the leading edge, decreasing levels on both suction and pressure surfaces, a rapid rise in values on the suction side where transition is observed, and a milder rise on the pressure side where velocity is increasing and acceleration is retarding transition. Acceleration, compressibility, transition, curvature effects are in play. There is no film cooling or roughness effect in this study. Shown are the results

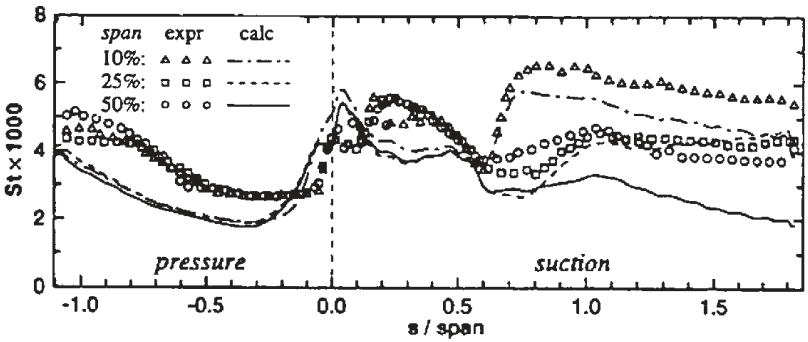

Figure 42: Predicted and measured Stanton number distributions for the blade. Reynolds number based upon inlet velocity and axial chord length = 1.0×10^6, exit Mach number = 0.98, inlet turbulence intensity = 7%. Experiments are with the liquid crystal technique; computations are with the 3D code RVC3D (from Giel *et al*. [66]).

of a complex array of effects on Stanton number. The figure also shows how the distribution varies from the mid-span region (50% span) to near the endwall (10% span). Clearly, 3D effects cannot be ignored in airfoil design.

3.4.1.4 Additional external heat transfer considerations Correlation-based heat transfer coefficients and heat transfer coefficients calculated using two-dimensional numeric codes may be improved upon by considering additional flow features that are not well modeled in two dimensions. They are considered under the general category of secondary flows and can have significant effects on heat transfer.

Factors that influence the near-wall flow field, such as skewing and mixing by secondary flows and with film cooling and leakage (or sealant) flows tend to influence heat transfer coefficients. Also, such effects as surface roughness or freestream turbulence (level and scale) significantly influence heat transfer.

3.4.1.5 Secondary flows Secondary flows within turbine passages are complex. Much research has been devoted to characterizing them. They are generally the result of pressure gradients induced by strong turning of the flow as it moves through the passage. This is expected at junctions between airfoils and endwalls or in regions of strong jetting, such as leakage flows or tip bypass flows. Several of the more important flows are highlighted below.

The endwall cross flow, as identified by Langston [67] in Fig. 43 is induced by the strong pressure gradient between the pressure side of the passage and the suction side of the passage. This is due to curvature of the streamlines within the passage. In the endwall boundary layer that resides within the passage, velocities are generally low and these pressure gradients create a movement of near-wall fluid from the pressure side of the passage to the suction side. The intensity of this cross flow is dependent on several factors including the degree of turning and the aspect ratio (the ratio of the passage height, or airfoil span, to the airfoil chord length).

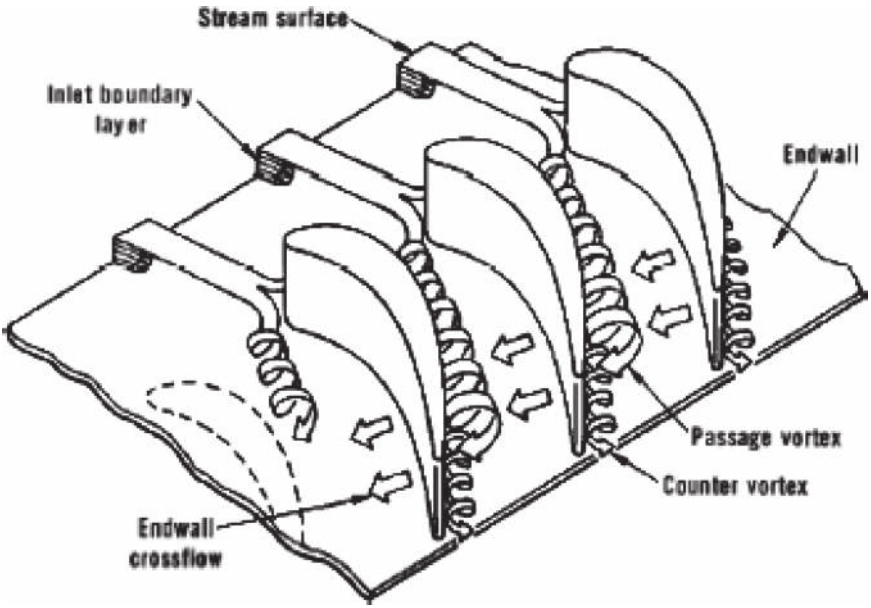

Figure 43: Secondary flows in the endwall region for a turbine airfoil row (from Langston[67]).

Another component of secondary flow in the passage is the horseshoe vortex, two legs of which are shown in Fig. 43. This structure begins at the leading edge of the airfoil at the junction between the airfoil and the endwall. The fluid stagnates against the leading edge of the airfoil. Since the approach flow near the endwall has a boundary layer, the stagnation pressure varies from a larger value at the outer edge of the boundary layer on the stagnation line and the minimum value at the endwall-airfoil leading edge junction. This pressure gradient at the leading edge drives the flow down the leading edge region toward the endwall (as shown in Fig. 43). The net result is a vortex that initiates at the leading edge of the airfoil and continues through the passage. If it were not for curvature of the passage, this vortex would assume a horseshoe shape. On the suction side of the airfoil, the vortex is quickly stretched by flow acceleration and begins to dissipate. On the pressure side, the vortex is influenced by the passage cross flow, which carries it to the suction side of the passage. There, it impinges against the suction side of the airfoil.

The passage flow augments the strength of the vortex. At the upper reaches of the pressure side leg of the vortex, the core passage flow velocity is high. The shear resulting from the interaction of the boundary layer flow (with the vortex embedded within it) with the core passage flow causes the vortex to grow in size and strength. The result is a much larger and stronger structure associated with this leg as it reaches the suction side of the passage, compared to the size and strength of the suction side of the horseshoe vortex. This pressure-side leg of the horsehoe vortex, which has been carried to the suction side, combines with the cross flow vortex (which is of the same rotational direction) to be called the passage vortex.

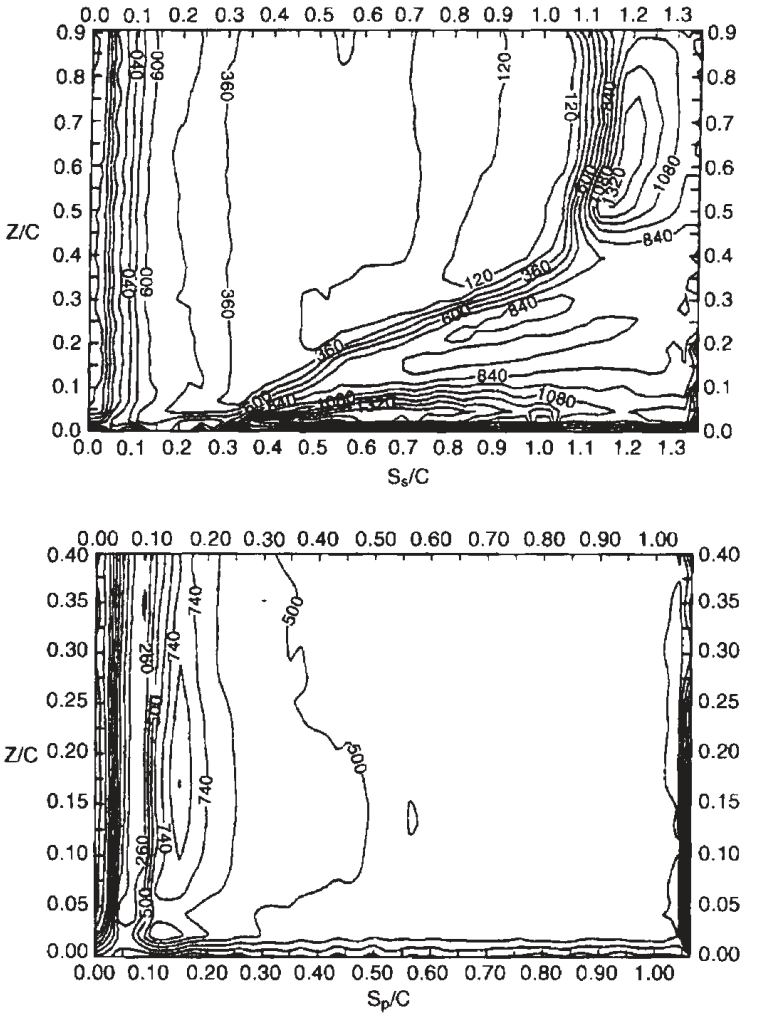

Figure 44: Detailed Sherwood numbers on blade suction and pressure surfaces near the endwall (from Goldstein *et al*. [68]).

Downstream, the passage vortex moves off the passage endwall and up the suction sidewall. Flow on the pressure side of the airfoil is drawn toward the endwall of the airfoil. Figure 44 shows mass transfer measurements in a cascade. With the analogy between mass and heat transfer, one can convert the mass transfer Sherwood number values, shown, to heat transfer Nusselt numbers. One can see on the suction side the effect on mass transfer of the vortex impinging on and traveling up the suction wall in the downstream portion of the passage. On the pressure wall, the Sherwood number distribution is rather two-dimensional, indicating that the passage vortex is carrying major components of the near-endwall region secondary flow away from the airfoil pressure surface.

The horseshoe vortex and passage vortex have a very significant effect on endwall heat transfer. These vortices bring hot flow from the core of the passage to the surfaces of the passage. Thus, in the regions over which the vortex passes, the surface heat transfer rates tend to be higher than in neighboring regions. The vortices also tend to mix the boundary layer fluid with the passage fluid, increasing heat transfer coefficients. In regions of high flow acceleration, there is a possibility of strong vortex stretching, with its associated dissipation, and some possibility of boundary layer relaminarization. This subject is addressed in Graziani *et al.* [69]. Figure 45 shows a representative distribution of Stanton numbers on the endwall and selected regions of the suction and pressure surfaces.

Correlations for estimating the effects of secondary flows on passage overall aerodynamic losses exist, but characterization of secondary flow effects on heat transfer coefficient distributions over the surfaces of the passage requires either measurements in a cascade facility as shown by Figs. 44 and 45, above, or rather complex and finely nodalized (to capture the heat transfer rates) 3D numerical simulations.

The blade tip region also induces secondary flow. The high pressure on the pressure side of the airfoil drives flow across the tip to a low-pressure region on the suction side. The tip leakage flow brings high temperature passage air through this tip region to mix with the passage air on the suction side of the passage as shown by Key and Arts [70] in Fig. 46. Shown also is a vortex on the suction side which is driven by the tip leakage flow. The effects that the sink flow into the tip gap has on the pressure side heat transfer and the jetting flow on the suction side has on the suction side heat transfer were measured by Metzger and Rued [71] and Rued and Metzger [72], respectively. The vortex on the suction side augments the heat transfer coefficient near the tip gap. The shape of this augmentation depends on the Reynolds numbers of the passage flow and tip gap flow.

3.4.1.6 Effect of leading edge shape The airfoil leading edge shape influences heat transfer distributions on the blade and endwall surfaces. Van Fossen and Simoneau [73] showed that elliptical cross-sections provide reduced heat transfer rates on the leading edge compared to those for circular cross sections. Furthermore, the heat transfer coefficient profile is more peaked at the stagnation point for the elliptical leading edge and the heat load downstream of the stagnation point is reduced from that of the circular cross section. The test pieces and representative data are shown in Fig. 47. The Frossling number was introduced previously. The values $Fr(0)$ were taken under low freestream turbulence conditions.

The leading edge shape at the airfoil to endwall junction can have a strong effect on the endwall heat transfer rate as shown computationally by Saha *et al.* [74]. Figure 48 shows the effect of one leading edge fillet.

3.4.1.7 Effect of surface roughness Turbine airfoils start out with a "smooth" (as-cast or as-coated) condition. With engine operation, the airfoil surface typically becomes rougher. Roughness may come about by dirt accumulation, surface corrosion and oxidation, erosion, spallation of TBC layers (often by thermal stress effects), and by material deposition, often by particles or condensables in the fuel.

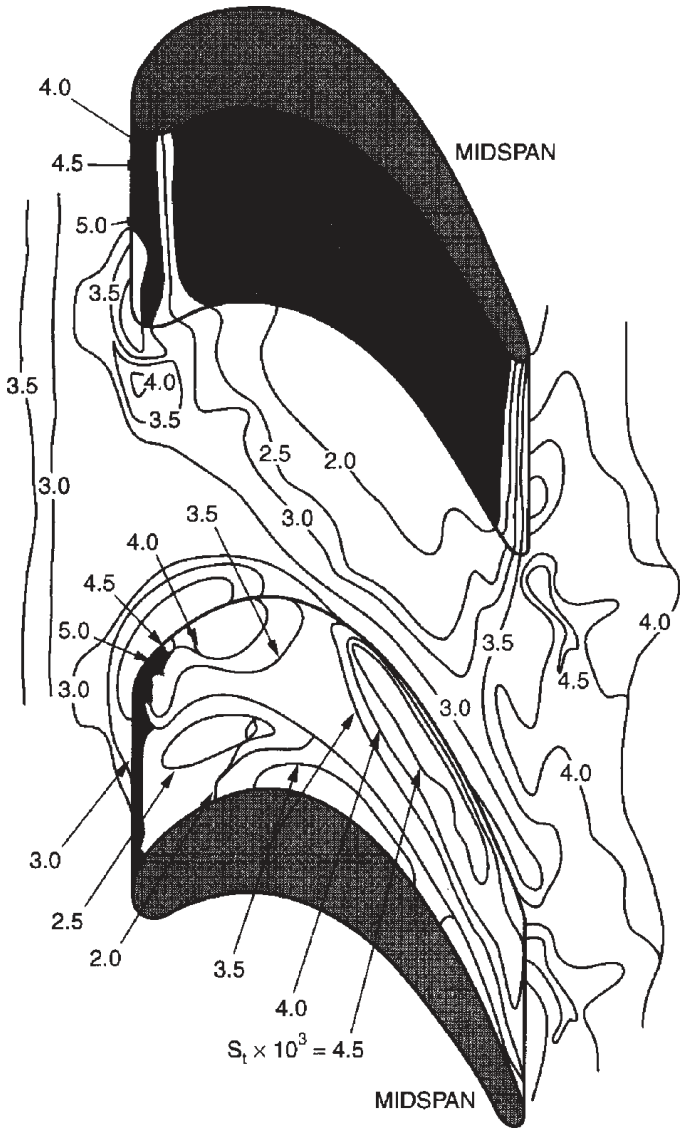

Figure 45: Endwall and blade surface Stanton number distributions for a thick boundary layer (from Graziani *et al*. [69]).

Different engines, operators, environments, materials and temperature histories affect how much roughness will develop and what shape the roughness will assume. Dirt accumulation is typically worse for a first-stage vane than for downstream airfoils, since this is the first stage in which the flow experiences strong streamline curvature and resulting separation of solids from the passage gas.

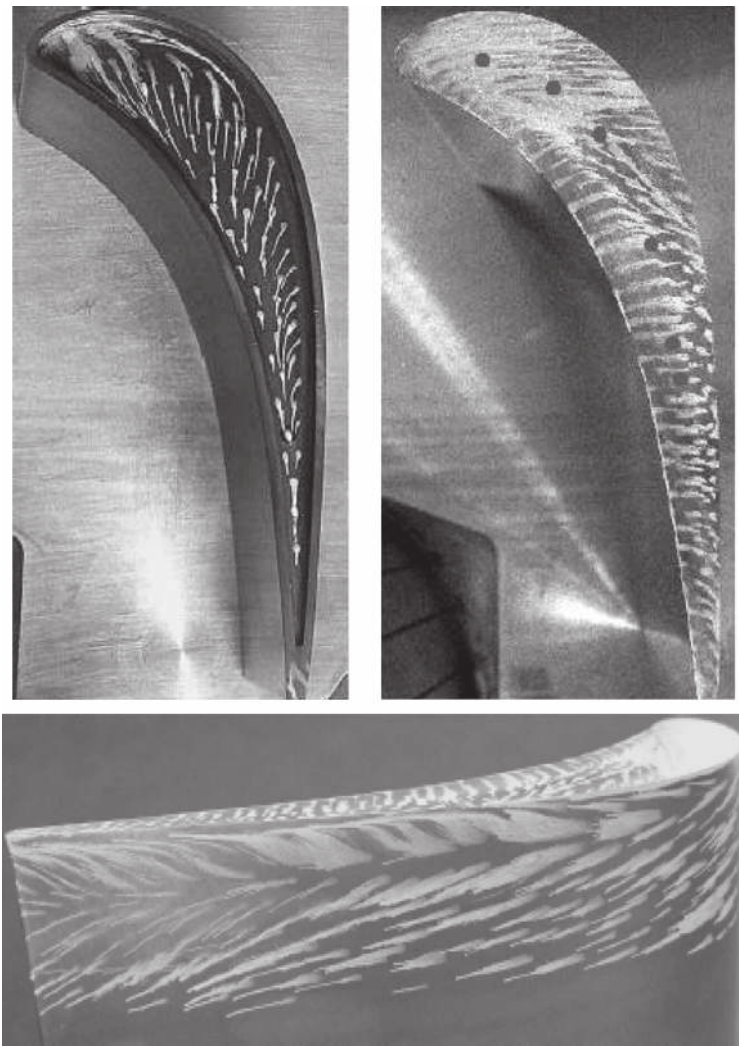

Figure 46: Visualization of tip clearance flow. The blade on the upper left has a squealer tip while the one on the upper right has a flat tip. The lower figure shows the vortex on the suction side, driven by the tip leakage flow (for the flat tip) (from Key and Arts [70]).

Effects of surface roughness on flow and heat transfer have been under study for many years, beginning with comprehensive experiments with sand-grain roughened walls and a single length scale for characterizing roughness. Roughness on the airfoil is not characterized well with uniform sand-grain roughness, however, since deposition and erosion do not occur uniformly. As found by Bons *et al.* [75], airfoils that have seen service show surface micro-geometry features caused by erosion, deposits, pitting, and TBC spallation, which are quite different from sand grain

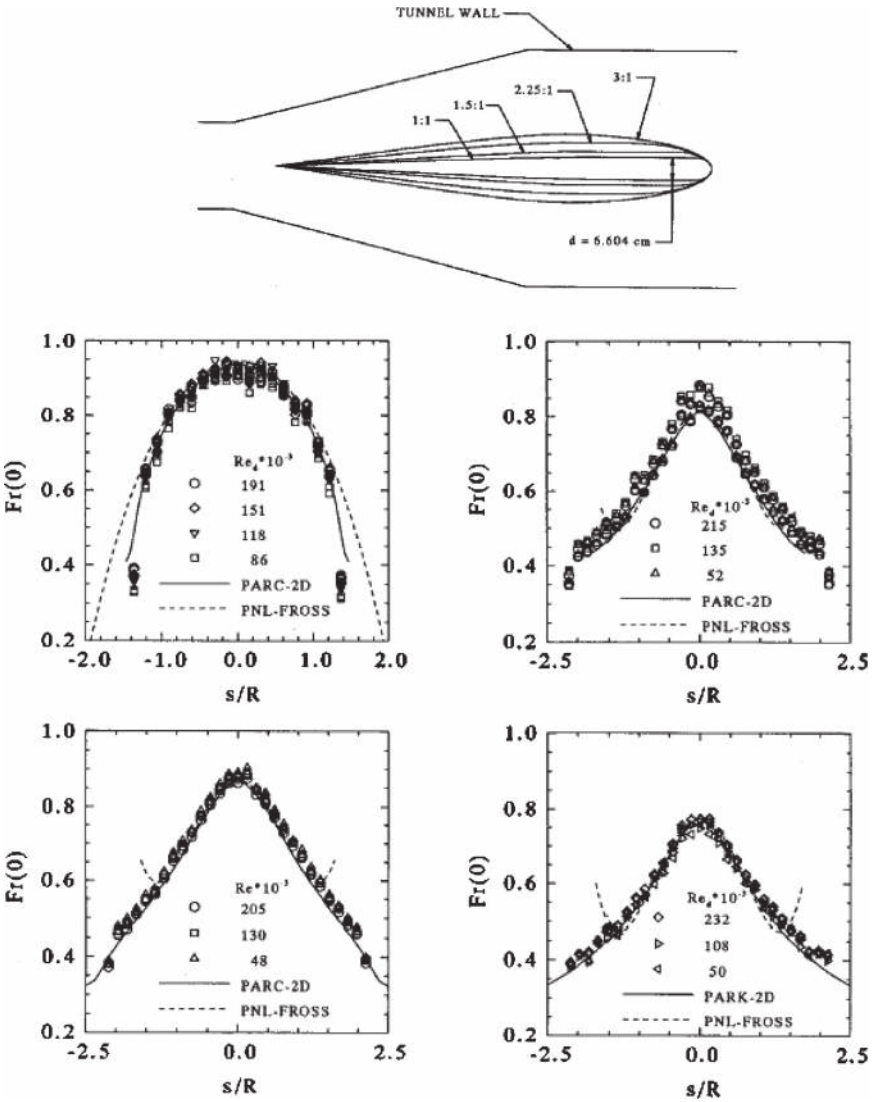

Figure 47: Model profile and low turbulence Frossling number distributions around leading edge compared to PARC-2D and Frossling solutions. Top: Model profile; upper left: 1:1 ellipse; upper right: 2.25:1 ellipse; lower left: 1.5:1 ellipse; and lower right: 3:1 ellipse. PAR-2D is a 2D numerical simulation code (from Van Fossen and Simoneau [73]).

roughness, and from one another. It would be expected that the different types cannot be modeled as an equivalent sand grain roughness. They note that for uncoated turbine airfoils, corrosive deposits and erosion are the primary causes of roughness, occurring near the pressure side tip and hub regions, while spallation is the dominant cause of roughness for coated airfoils. The spallation effect was pronounced near the

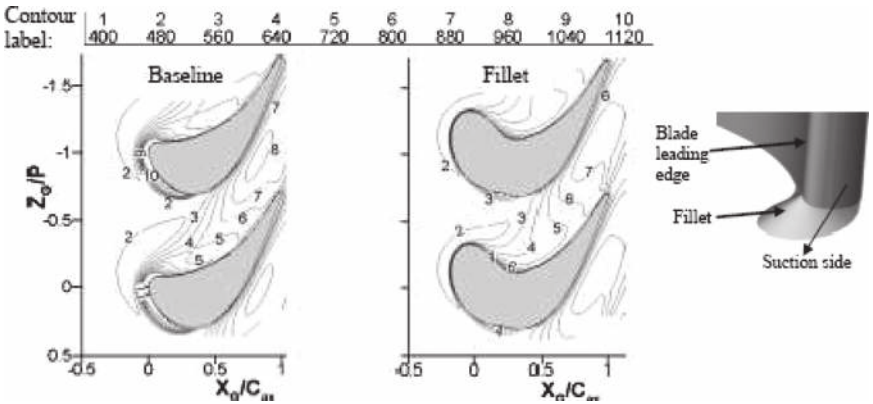

Figure 48: Computational results of Nusselt numbers, *Nu*, along the endwall of baseline and filleted geometries (from Saha *et al*. [74]).

leading edge on the suction side. Documentation of the evolution of surface roughness under engine conditions and the effects on heat transfer is given by Wammack *et al.* [76] and Bons *et al.* [77]. Discrete roughness, as found on turbine airfoils, has been simulated in flat-plate situations using cones [78], pedestals [79], cylinders [80], and hemispherical elements [81]. All these studies indicate that enhancement in Stanton number (*St*) can be as much as 60% over the smooth-surface value, while the friction factor may increase by up to a factor of 3. Clearly, the Reynolds analogy between momentum transport and heat transfer is not valid. Form drag on roughness elements, one component of pressure drop, has no equivalent heat transfer mechanism. In cases with wall curvature, roughness is a strong factor influencing heat transfer and skin friction [83]. The influence of roughness can be seen on both sides of the airfoil. However, its effect tends to be more pronounced on the suction side surface. On the suction surface, the roughened surface tends to force an earlier transition causing elevated heat transfer coefficients just downstream of the leading edge. Enhanced heat transfer coefficients can also be seen in the portion of the airfoil downstream of the leading edge. An example of the effects of roughness on airfoil heat transfer is shown by Hoffs *et al.* (83) in Fig. 49. Clearly, the roughness effect is an earlier transition to turbulence and a more rapid development of the turbulent boundary layer on the suction surface. The effects on the laminar boundary layer on the suction surface and on the entire pressure surface are weak. A similar study but with a different airfoil profile shape was done by Bunker [84]. Again, the main effects of roughness are seen at the leading edge and at locations influenced by transition to turbulence. In this case, the pressure surface is more strongly affected by roughness (see Fig. 50).

3.4.1.8 Effect of freestream turbulence The combustor exit flow typically shows a high level of freestream turbulence with large length scales, as discussed

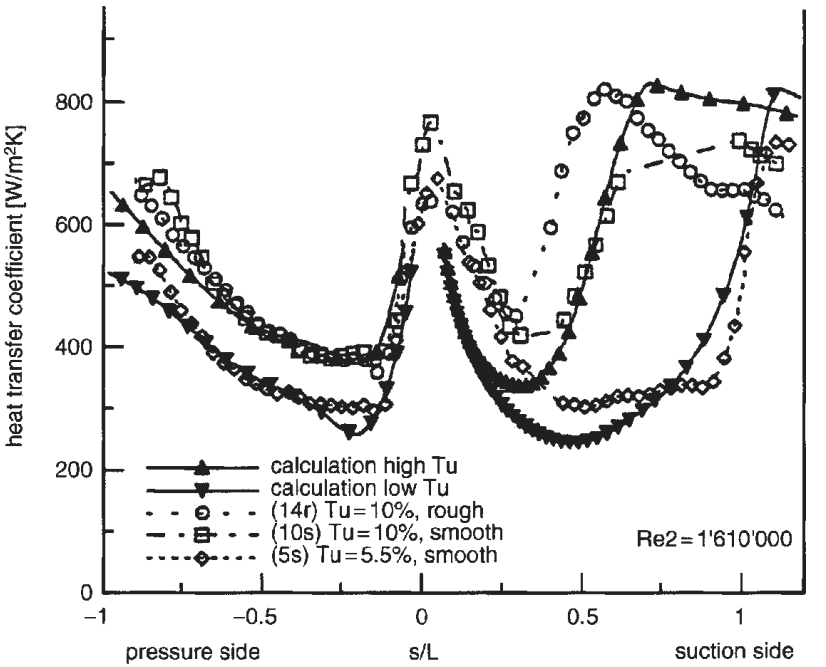

Figure 49: Effect of surface roughness and free-stream turbulence on airfoil heat transfer coefficient distribution (from Hoffs *et al*. [83]).

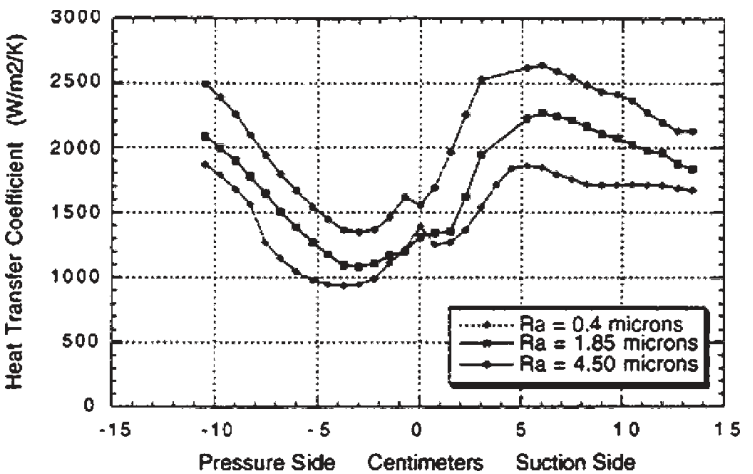

Figure 50: Effect of surface roughness with $Re_{cx} = 4.7 \times 10^6$ and $Tu = 9\%$ (from Bunker [84] , *Ra* is the centerline average roughness).

above. Turbulence can have a significant effect on heat transfer coefficients on the turbine airfoils. This turbulence can affect the heat transfer at the leading edge, the location of laminar-turbulent transition, and to a lesser extent in engine flows, the turbulent flow heat transfer.

Elevated freestream turbulence induces an earlier transition to turbulence, as was shown in the transition correlation of Mayle (eqn (27)) and the airfoil heat transfer data in Fig. 49. The effects of elevated freestream turbulence on leading edge heat transfer are captured in the correlations of Van Fossen *et al*. (eqn (28)) and Dullendopf and Mayle (eqn (30)). Elevated freestream turbulence will enhance convective heat transfer coefficients in turbulent boundary layers. One correlation for this is given as a new definition of Stanton number:

$$St' = h / \rho C_p u'_{max} \tag{37}$$

by Maciejewski and Moffat [85], [86]. Setting this value to 0.024 is a rough approximation to the curve they show. Han *et al.* [1] suggest that results in the literature support this approximation. The velocity scale is found by surveying across the boundary layer at the streamwise position of interest to find the maximum value of the rms fluctuation of streamwise velocity, u'_{max}. An approximate method for attaining that value is to begin with an upstream level of turbulence intensity and, by assuming a concept called "frozen turbulence" compute the local value of u'_{max} as:

$$u'_{max,\,local} = \frac{TI_{upstream}\bar{U}_{upstream}}{\bar{U}_{local}} \tag{38}$$

The upstream station may conveniently be the combustor exit or the passage inlet, whichever has reliable turbulence intensity data. Usually turbulence intensity levels,$TI \equiv u/\bar{U}$, in the regions where this would be applied to airfoil heat transfer are in the vicinity of 10% or greater.

The effects of freestream turbulence on airfoil surface heat transfer are documented in several studies in the literature. It is generally accepted that both level and scale of turbulence are important. Generally, the main effects are on the leading edge heat transfer, as discussed above, and on portions of the airfoil which are influenced by transition to turbulence. Because each airfoil shape has a particular pressure profile and transition is strongly dependent on streamwise spatial acceleration, there is no simple and general means for applying turbulence level and scale to correlations for suction and pressure surface heat transfer coefficient distributions. Experimental evidence with the proper airfoil shape or numerical simulation is necessary. Unfortunately, numerical simulation is correct only if the transition is computed correctly and to date, no transition model is available that accurately accounts for all the parameters that influence transition: freestream turbulence level and scale, roughness, pressure profile, curvature, film coolant injection, etc. An example of experimental evidence of the effects of freestream turbulence is offered by Ames [87] (see Fig. 51). The baseline case is with a low turbulence level, the "grid" case is with a grid of square bars and the two "comb" cases are with two mock-up arrangements of different combustor and combustor-to-turbine transition

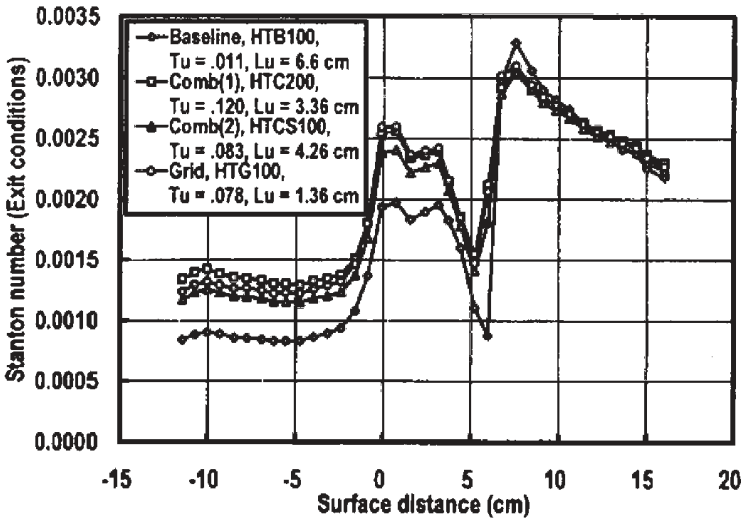

Figure 51: Effects of turbulence on Stanton number distribution, Re_{ex} = 790,000 (from Ames [87]).

duct geometries. Each case has a specific combination of turbulence level and scale. The turbulence scale is the energy length scale discussed previously.

3.4.2 Film cooling

3.4.2.1 Objectives of film cooling Film cooling by injection of coolant through porous walls, slots, and holes has been used for fifty years as a means of protecting gas turbine engine surfaces from adjacent hot gas streams. With film cooling, the surfaces are covered with a layer of relatively cool air. The effectiveness of protection is dependent upon the amount of coolant provided, the coolant supply temperature, and how the coolant interacts and mixes with the hot gas stream into which it is injected. In design, one wishes to determine where and how film cooling will be introduced so that each engine component is operating at the appropriate temperature. Of course, this is done in coordination with the internal cooling design. Film cooling design is not easy, for injection is to a gas turbine flow path environment that has a very complex flow field.

3.4.2.2 The transpired boundary layer Transpiration cooling is the simplest form of film cooling. It provides uniform injection of coolant flow though a porous wall. The injection temperature is the wall temperature. Injection will cause the boundary layer to grow, and the wall shear stress to drop, with distance from the beginning of injection. If the injection rate is large enough or blowing length is long enough, the shear stress approaches zero and the injected flow blows the passage flow off the wall. This would be a case of excellent film cooling coverage, but the coolant flow demand may be excessive and aerodynamic losses associated with injection may be substantial.

Though transpiration cooling appears attractive and some combustor liner cooling designs approach it, it is not the preferred method for film cooling of gas turbine airfoils and endwalls. Since film cooling air is combustor bypass air that had been ingested into the compressor, it contains dirt and debris that would fill the fine pores of a transpiration cooled surface. Also, airfoils fabricated with porous walls may be too fragile for the duty they are called upon to serve.

3.4.2.3 Full coverage film cooling A reasonable extension of transpiration cooling is to simply open up the pore sizes to become holes distributed uniformly over the surface. This is called "full-coverage film cooling," a geometry that is often approached in practice (see Fig. 3). Several changes result from transpiration cooling. First, the delivery holes are larger than the pores of the transpiration-cooled surface. It is not reasonable to assume that the injected flow will enter the boundary layer at the wall temperature. Thus, a third temperature is introduced to the problem, the coolant temperature, T_c, yielding three relevant temperatures: T_s, T_∞ and T_c, for surface, external flow, and coolant, respectively. A second characteristic, which separates discrete hole cooling from transpiration cooling is the degree of mixing between the gas stream flow and the injected flow. Since the coolant flow enters the gas passage stream as discrete jets (see Fig. 52), the mixing region becomes highly three-dimensional, the emerging jet appears as a flow blockage to the approaching gas stream flow and the mainstream is forced to divert around and over the injected flow. An undesirable outcome is much stronger mixing of the injected flow and the gas stream flow. This mixing, of course, degrades the performance of film cooling. This also leads to increases in aerodynamic losses and some augmentation of surface convective heat transfer coefficients. If the injection

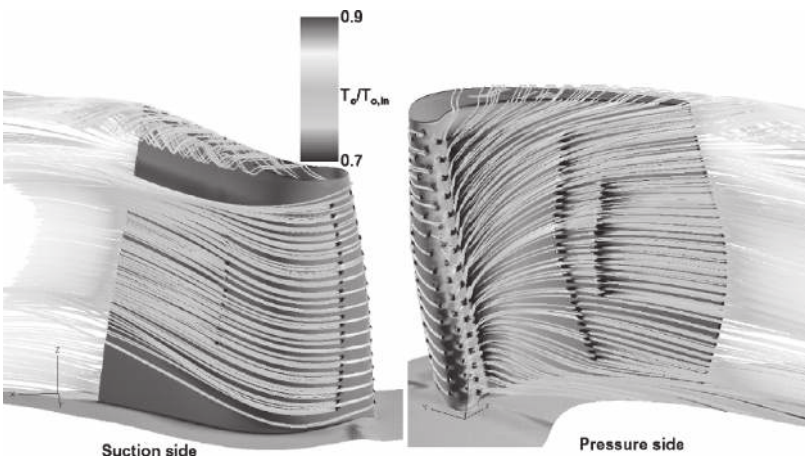

Figure 52: Streamlines emanating from holes over the cooled blade surface (from Garg [88]).

rate becomes high enough, the jets would "tunnel through" the boundary layer flow and the cooling effectiveness becomes quite poor, the aerodynamic losses are high, and the heat transfer coefficients are substantially enhanced.

3.4.2.4 Describing film cooling in terms of the adiabatic wall temperature When film cooling is being applied, the heat transfer analysis must be modified. Having three temperatures raises a question as to how the heat transfer coefficient might be described in terms of heat source (passage) and sink (wall) temperatures. In a traditional boundary layer flow, heat transfer rates are given by Newton's law of cooling (simply a definition of the heat transfer coefficient, h):

$$q'' \equiv h\left(T_{\mathrm{w}} - T_{\infty}\right) \tag{39}$$

In the case of discrete-hole film cooling, h is modified, somewhat, by the injected flow. This is particularly true immediately downstream and in the near vicinity of the injection point. Farther downstream, one can often use, with little error, the h value one would expect without film cooling. In the case of discrete-hole film cooling, the thermal driving potential becomes the difference between the effective temperature within the zone where the coolant and passage flows mix and the wall temperature:

$$q'' \equiv h(T_{\mathrm{film,\,effective}} - T_{\mathrm{w}}) \tag{40}$$

The effective temperature, $T_{\mathrm{film,effective}}$, is determined by a study of mixing of external flow and the injected flow. It is dependent upon the flow field. Correlations are formulated to isolate "h" and $T_{\mathrm{film,effective}}$ by first determining $T_{\mathrm{film,effective}}$ in the absence of wall heat transfer (set the wall to be adiabatic) but under the same flow conditions. Thus, a reasonable value for $T_{\mathrm{film,effective}}$ could be T_{aw}, the wall temperature established when the wall is adiabatic. To continue the separation, one then determines "h" with a heated wall but with the "film cooling" and gas passage flow temperatures being the same. This "h" value is altered by injection solely via mixing due to the interaction of the two streams. This value is usually normalized as the Stanton number:

$$St = \frac{h}{\rho u_{\infty} c_{\mathrm{p}}} \tag{41}$$

or Nusselt number

$$Nu_x = \frac{hx}{k} \tag{42}$$

The Nusselt number would require an appropriate choice of length scale, perhaps x, the streamwise distance from the hole.

The adiabatic wall temperature is normalized as the film cooling effectiveness:

$$\eta = \frac{T_{\infty} - T_{\mathrm{aw}}}{T_{\infty} - T_{\mathrm{c}}} \tag{43}$$

The effectiveness is 1.0 when the adiabatic wall temperature is the coolant temperature and zero when it is the freestream temperature. We therefore develop expressions for η and St/St_0 (the subscript "0" indicates the situation in which there is no film cooling present) in terms which capture the effects of:

- Geometric features: slot width, hole size, distance from the injection point, radius of streamwise curvature, hole pattern geometry parameters, hole delivery channel geometry parameters, etc.
- Flow parameters: mass fluxes of injection and gas passage flows, momentum fluxes of injection and gas passage flows, boundary layer thickness at the point of injection, velocity distribution of the emerging film cooling flow, turbulence intensity levels and length scales in the gas passage flow and the coolant flow, parameters which capture secondary flow features within the gas passage, etc., and
- Fluid properties: density, viscosity, specific heat, etc.

3.4.2.5 Discrete hole injection parallel to the surface A simple film cooling realization is through a slot oriented so that injection is tangent to the wall. This is a discrete injection with no wall-normal component of velocity component. An analysis of it from Librizzi and Cresci [89] yields the following expression:

$$\eta = \frac{1}{1+(c_{p,\infty}/c_{p,c})\left[0.329\left(4.01+\varsigma\right)^{0.8}-1\right.} \tag{44}$$

where

$$\varsigma = \frac{x}{s}\frac{\rho_\infty u_\infty}{\rho_c u_c}\left(\frac{\mu_c}{\mu_\infty}\left[\frac{\rho_c U_c s}{\mu_c}\right]\right)^{-1/4} = \frac{x}{Ms}\left(\frac{\mu_c}{\mu_\infty}\left[\frac{\rho_c U_c s}{\mu_c}\right]\right)^{-1/4} \tag{45}$$

Once we establish the origin of x, we can compute η from the correlation. The most important parameters to the correlation are the mass flux ratio, $M = \rho_c u_c/\rho_\infty u_\infty$ and the streamwise distance from the hole in terms of the slot length, x/s. If we are sufficiently far from the injection zone, we might assume that h is unaffected by injection.

Tangential slot injection is usually not applied for airfoil surface film cooling because of the difficulty of implementing a slot into the airfoil geometry and because of the reduction of airfoil strength it would create. Some combustor cooling schemes have injection geometries that approach tangential injection, however.

3.4.2.6 Injection with a wall-normal component of momentum A more practical injection geometry is discrete injection with single, double, or several rows of holes (see Fig. 3). Though injection may be over a short streamwise distance, protection continues downstream of the injection zone until the coolant is mixed out. Downstream coverage by injection through rows of discrete holes is visible in

Fig. 52. Also visible is how the various coolant paths are influenced by secondary flows in the hub and tip regions.

If the coolant has a component of momentum flux in the wall-normal direction, the wall–normal momentum flux relative to the gas stream momentum flux may be a parameter of interest for it might suggest greater penetration of the coolant flow into the gas passage flow. This would influence the mixing process. One might expect that a value of wall-normal momentum flux approaching the gas stream momentum flux evaluated at the elevation where the interaction of the two streams is most intense would signal a possibility of coolant lift-off (or separation) from the surface, with a corresponding precipitous degradation of cooling performance. So long as the injected jet is not lifting off the wall, variations on the slot injection correlation given above can be applied to hole injection to give an estimate of the laterally averaged effectiveness. One could develop film cooling design correlations of the form of eqn. (44) where x/s is the streamwise distance in terms of the hole diameter, $s = d$, or effective slot length, $S_e = \pi d^2/4p$ for a single row of holes (p is the pitch). Of course, the actual processes are complex, so specific forms of the equation apply to specific geometries and sets of flow conditions. Such correlation forms are for the lateral-averaged effectiveness. Actual distributions are quite two-dimensional, as shown in Fig. 53.

When there are more than one row of film cooling holes, $i > 1$, and the blowing is sufficiently low that the coolant is not separating from the surface, the following superposition expression can be used for an approximation to the net film effectiveness:

$$\eta_f = \sum_{i=1}^{N} \eta_{f_i} \left[\prod_{j=0}^{i-1} (1 - \eta_{f\,j}) \right] \tag{46}$$

3.4.2.7 Net benefit of film cooling Film cooling reduces the source temperature for convective heat transfer from the gas to the wall, but it also augments the convective heat transfer coefficient, h. It will result in an overall thermal benefit if the net of the two is a lower heat flux $q''/q' < 1.0$.

$$\frac{q''}{q_o''} = \frac{h\,(T_f - T_w)}{h_o(T_g - T_w)} = \frac{h}{h_o}\left(1 - \eta \frac{T_g - T_c}{T_g - T_w}\right) \tag{47}$$

where q" is the heat flux with film cooling q_o is the heat flux without film cooling h is the heat transfer coefficient with film cooling h_o is the heat transfer coefficient without film cooling T_w is the local wall temperature T_c is the coolant temperature, and T_g is the mainstream gas temperature.

The net heat flux ratio therefore depends upon the engine operational parameters, T_c/T_g, T_w/T_g, and h_0, as well as the film cooling parameters, η and h/h_0.

3.4.2.8 Hole shape and orientation effects The film cooling hole shape is important as it determines the film coverage downstream of a row of cooling holes

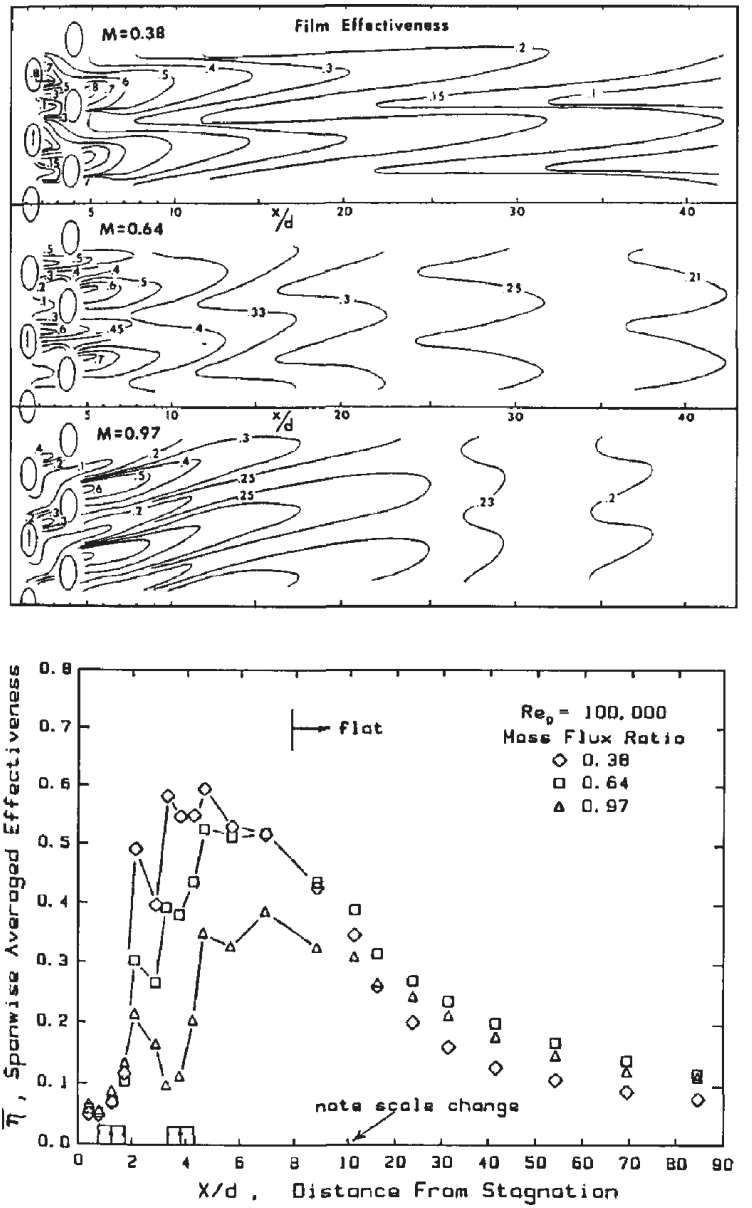

Figure 53: Detailed and spanwise-averaged film effectiveness distributions for three injection rates. The contours in the upper figure are fractions, i.e. the center contour is 0.30. This figure shows effectiveness values for injection through holes of diameter d on a half-cylinder leading edge of diameter *D*. Beginning at 90° of arc from the stagnation line are flat plates representing the suction and pressure sides. The diameter ratio, *D*/*d* is 10. The Reynolds number, Re_D, is based on the incidence velocity and the leading edge diameter (graphics from Mick and Mayle [90]).

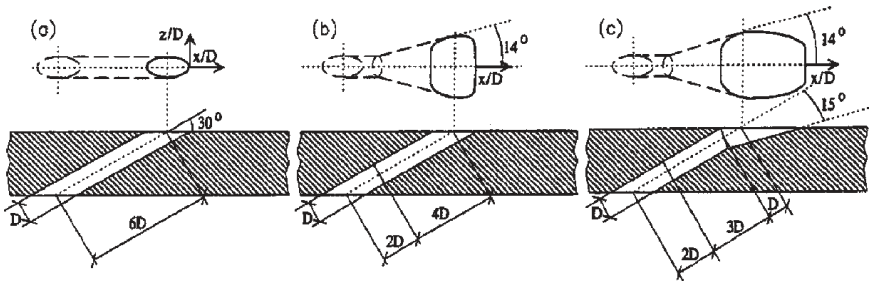

Figure 54: Some shaped hole configurations (from Gritsch *et al*. [92]).

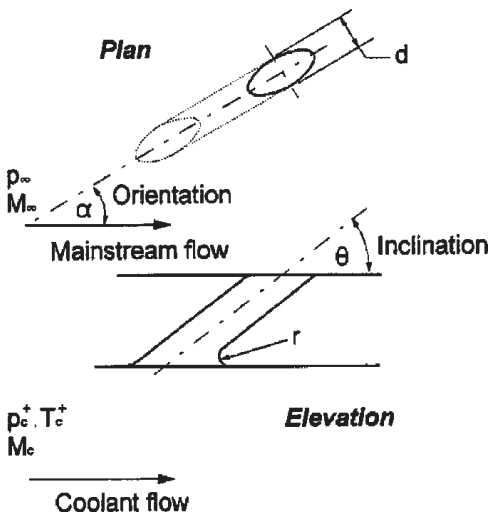

Figure 55: Film cooling geometry and flow parameters (from Hay and Lampard [93]).

and the degree of mixing between coolant and passage flow. Common shapes are round holes or shaped holes, such as expanded (or fan-shaped) holes or laid-back holes (see Fig. 54). Shaped holes are designed to allow the flow to diffuse as it exits the hole. This improves the coverage of the flow. Conical holes have also been applied. Common orientations are in-line, lateral, and compound. With lateral injection, the hole axis is perpendicular to the oncoming flow ($\alpha = 90°$) in Fig. 55. Compound injection is usually with a $\alpha = 45°$, half-way between in-line and lateral. The holes are inclined relative to the surface, generally with an angle of 30–35° (θ in Fig. 55). This is a compromise between the desire to introduce the flow parallel to the surface and ease of manufacturing. One parameter for discussing the film coverage is the ratio of breakout, t, to film hole pitch, p, as shown in Fig. 56. Generally, larger ratios have better film protection, though if they are

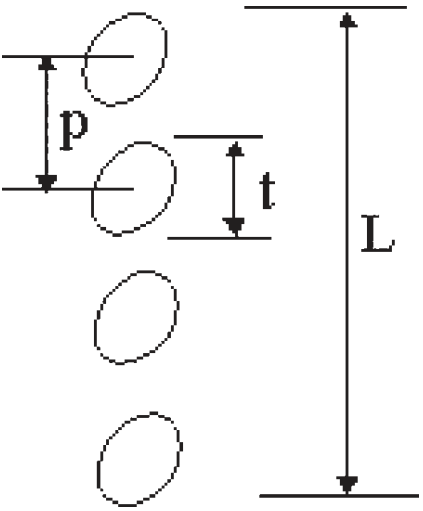

Figure 56: Parameters used to describe coverage.

made larger by swinging the axis of the hole toward the lateral direction, there may be a point at which strong mixing begins to reduce the coverage.

The flow rate through the hole is determined by the pressure gradient across the hole and the resistance to flow through the hole and delivery line. This is described in terms of a discharge coefficient:

$$c_{\mathrm{d}} = \frac{\dot{m}_{\text{ actual}}}{\dot{m}_{\text{ ideal}}} = \frac{\dot{m}_{\text{ actual}}}{A\sqrt{2p(p_{\mathrm{t,c}} - p_{\mathrm{s}})}} \tag{48}$$

where $P_{\mathrm{t,c}}$ is the total pressure in the coolant supply plenum to the hole and P_{s} is the static pressure over the hole. It is an important parameter for setting the cooling flow rate from the hole. The value of the coefficient will depend on the hole geometry and also the conditions, which exist upstream and downstream of the cooling hole. An example comes from Burd and Simon [91] (see Fig. 57), which shows the effects of hole orientation and direction of the supply flow as it approaches the hole. Gritsch *et al.* [92] showed that when cross flow is applied to the channel from which a cooling hole receives its flow, the discharge coefficient of the hole tends to increase (see Fig. 58). At high pressure ratios, shaped cooling holes show less of an increase. This is due to the pressure recovery produced by the diffusing portion of the hole.

3.4.2.9 Obstructions During operation, there is a potential for deposits (dirt or condensed material carried in the passage gas) to impinge upon the surface of the airfoil. In time, these deposits may obstruct the film cooling holes. Dirt may accumulate where streamline curvature is strong so that particles separate from the flow and impinge upon the surface. Also, local wall shear stresses are low enough that the particles that impinge are inclined to stay. Build-up by condensation of condensable matter in the passage gas is expected where the passage gas is near a

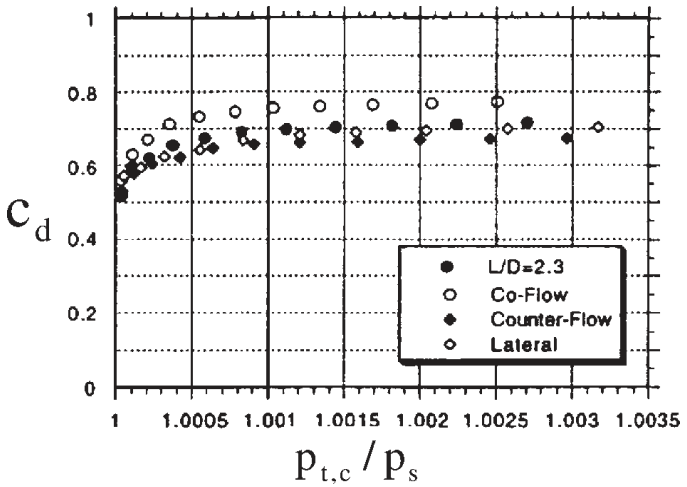

Figure 57: Film cooling discharge coefficients for cases in which there is no momentum of the fluid in the supply plenum (cases 1 and 4), momentum parallel to and in the direction of the passage flow (case 2), and in the opposite direction to the passage flow (case 3). For all, $L/D = 2.3$. Cases 1, 2, and 3 have in-line injection and case 4 has lateral injection (graphics from Burd and Simon [91]).

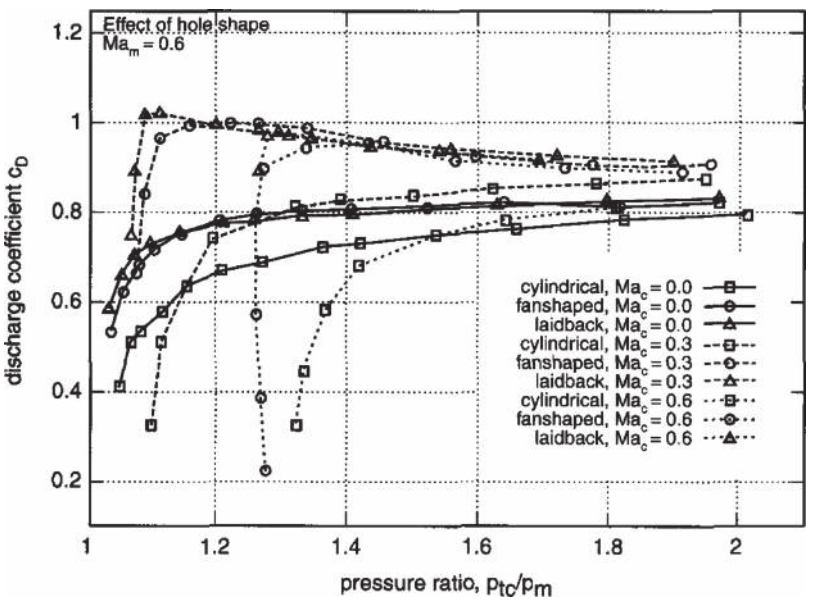

Figure 58: Effect of hole shape on discharge coefficients (graphics from Gritsch et al. [92]). Flow rates for the mainstream and coolant in the supply plenum are given in terms of Mach numbers, Ma_m and Ma_c, respectively.

locally cool wall section and shear stresses are low. This can be near the leading edges of film cooling holes.

3.4.2.10 Film cooling design As noted, film cooling is influenced by many effects (listed above). No simple correlation exists of the form of eqns. (44) and (45) that appropriately captures all effects in a general. Accurate correlations require measurements in facilities that capture all the important effects, or similarly complete numerical simulations must be conducted.

Film cooling on the leading edge is important, as the leading edge often has the highest heat load of the turbine. As noted above, freestream turbulence level and scale have strong effects in the leading edge region and the radius of curvature strongly affects the acceleration field and therefore the coolant interaction with the approach flow. Since the boundary layers in the leading edge region are thin, roughness and deposition can strongly influence performance. In general, for the leading edge with a multiple row of holes ("a showerhead"), the film superposition model discussed above is not used, for the mixing with the passage flow is too intense.

Correlation of film cooling data on the pressure side must account for the rapid decay in film cooling effectiveness due to concave curvature, free stream turbulence level, and pressure side particular pressure profile.

Correlations on the suction side must account for the slower decay of film cooling performance due to the more stable, accelerated boundary layer, and convex curvature. Again, it should be done for each particular design.

3.4.2.11 Film cooling on the tip The tip of the airfoil is difficult to cool for its geometry can change considerably due to oxide development, erosion and intense mixing of coolant and passage flow in the complex secondary flow discussed above. There is a substantial pressure difference between the pressure and the suction sides of the airfoil. This leads to high tip leakage flow and it associated mixing of the coolant. This effect is usually strongest at the mid-axial chord of the airfoil, close to the highest curvature point of the airfoil. In general, concentration of tip film cooling holes in this area can address potential tip oxidation and burning problems. As noted above, there is strong vorticity on the suction side of the blade near the tip, as driven by the tip leakage flow. These vortices penetrate radially and circumferentially quite far into the passage near the suction wall. It is therefore necessary to include dedicated film cooling in this tip region.

3.4.2.12 Film cooling on endwalls Endwall film cooling and heat transfer are strongly influenced by secondary flows in the gas path. Such secondary flows will dictate the position of the film holes on the platform.

Freidrichs *et al.* [94] documented a representative film cooling effectiveness distribution on the endwall of a large-scale, low-speed cascade (see Fig. 59). Results indicate a large region of the pressure side leading edge that remains uncooled. The passage vortex and endwall secondary flows sweep coolant from the pressure side to the suction side and can disturb the mid passage coolant. Although specific results will vary significantly from one configuration to the next, the study indicates that cooling holes placed near the passage pressure side may be expected to produce little benefit. Figure 52 shows the effects of tip and

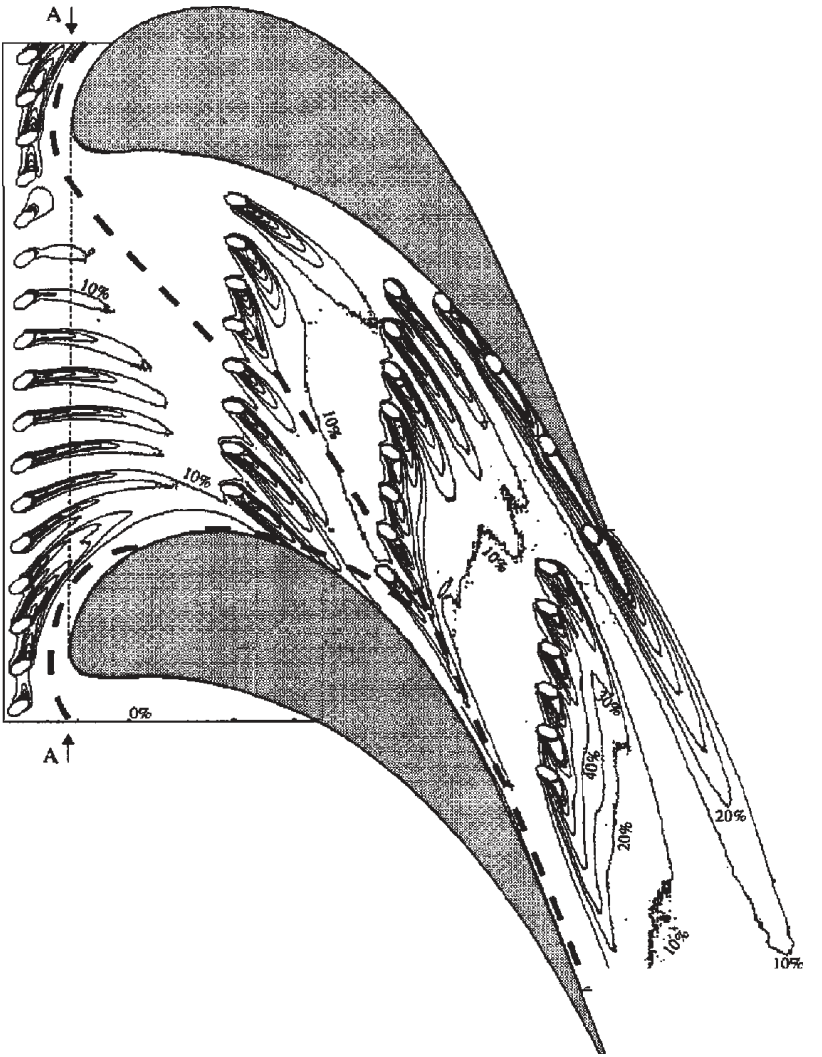

Figure 59: Endwall film cooling effectiveness distributions (graphics from Friedrichs *et al*. [94]).

endwall secondary flows on film cooling. Much of the discussion of endwall secondary flows in Section 3.4.1.5 can be applied toward making choices regarding film cooling injection hole locations on the endwall.

4 Concluding remarks

Important aspects of gas turbine hot gas path heat transfer technology have been reviewed. In some aspects, preliminary designs can proceed with rather simple

correlations, such as that presented for heat transfer on the leading edge. In most design aspects, the flow is too complex and heat transfer is influenced by too many factors for application of any general correlations. Thus, in support of engine design, (1) information in the literature is studied and interpreted; (2) measurements in cascades or other flow rigs which simulate the engine geometry and flow conditions of interest are taken and interpreted; (3) detailed calculations are made and the computed results are interpreted and; ultimately, (4) prototype engines are constructed, instrumented, operated, and examined for indications of excessive thermal loading. All of these steps require a strong understanding of the fundamental principles which govern flow and heat transfer in the gas path. Experiments and computations never include all effects; thus, an understanding of the physics is needed in making experimental or computational setup choices.

Though reliance on computations is rising, the art of computation is still encumbered with unanswered questions regarding computation of transition to turbulence and estimation of turbulent transport.

The objective of this chapter is to acquaint the designer with many important features of flow and heat transfer in the gas path that are to be considered when entering the literature, preparing experiments and computer models, and interpreting the information gathered.

References

[1] Han, J.-C., Dutta, S. & Ekkad, S., *Gas Turbine Heat Transfer and Cooling Technology*, Taylor Francis: New York, NY, 2000.

[2] Lakshminarayan, B., Turbulence modeling for turbomachinery flows (Section 5.2, Chapter 5). *Fluid Dynamics and Heat Transfer of Turbomachinery*, John Wiley & Sons: New York, NY, pp. 362–375, 1996.

[3] Drummel, H.-G., LeMeiux, D.H., Voigt, M. & Zombo, P.J., Online monitoring of gas turbine power plants, Siemens Power Generation Technical Paper, 2005.

[4] Cumpsty, N., *Jet Propulsion*, Cambridge University Press, Cambridge, UK, 1997.

[5] Goldstein, R.J., Lau, K.Y. & Leung, C.C., Velocity and turbulence measurements in combustion systems. *Experiments in Fluids*, **1**, pp. 93–99, 1983.

[6] Moss, R.W. & Oldfield, M.L.G., Measurement of hot combustor turbulence spectra, ASME paper 91-GT-351, 1991.

[7] Goebel, S.G., Abuaf, N., Lovett, J.A. & Lee, C.P., Measurements of combustor velocity and turbulence profiles, ASME paper 93-GT-228, 1993.

[8] van Fossen, G.J. & Bunker, R.S., Augmentation of stagnation heat transfer due to turbulence from a DLN can combustor, ASME paper GT-2000-215, 2000.

[9] Ames, F.E., Wang, C. & Barbot, P.A., Measurement and prediction of the influence of catalytic and dry low NO_x combustor turbulence on vane surface heat transfer. *Journal of Turbomachinery*, **125**, pp. 210–220, 2003.

[10] Povey, T., Chana, K.S., Jones, T.V. & Hurrion, J., The effect of hot-streaks on HP vane surface and endwall heat transfer: An experimental and numerical study, ASME paper GT2005-69066, 2005.

[11] Piggush, J. & Simon, T.W., Flow measurements in a first stage nozzle cascade having endwall contouring, ASME paper GT2005-68340, 2005.
[12] Hancock, P.E. & Bradshaw, P., The effect of free-stream turbulence on turbulent boundary layer flow and heat transfer. *Journal of Fluids Engineering*, **105**, p. 284, 1983.
[13] Oke, R.A., *Measurements in a Gas Turbine First Stage Nozzle Guide Vane Cascade with Film Cooling and Endwall Contouring*, PhD Thesis, Mechanical Engineering Department, University of Minnesota, 2001.
[14] Ames, F.E., The influence of large-scale high-intensity turbulence on vane heat transfer. *Journal of Turbomachinery*, **119**, pp. 23–30, 1997.
[15] Chana, K.S., Hurrion, J.R. & Jones, T.V., The design, development and testing of a non-uniform inlet temperature generator for the QinetiQ transient turbine research facility, ASME paper GT2003-38469, 2003.
[16] Viskanta, R., Heat transfer to impinging isothermal gas and flame jets. *Experimental Thermal and Fluid Science*, **6**, pp. 111–134, 1993.
[17] Goldstein, R.J., Behbahani, A.I. & Heppelmann, K.K., Streamwise distribution of the recovery factor and the local heat transfer coefficient to an impinging circular air jet. *International Journal of Heat and Mass Transfer,* **29**, pp. 1227–1235, 1986.
[18] Kelso, R.M., Lim, T.T. & Perry, A.E., An experimental study of round jets in crossflow. *Journal of Fluid Mechanics*, **306**, pp. 111–144, 1996.
[19] Lee, S.W., Lee, J.S. & Ro, S.T., Experimental study on the flow characteristics of streamwise inclined jets in crossflow on flat plate. *Journal of Turbomachinery*, **116**, pp. 97–105, 1996.
[20] Adolfson, D.A., Simon, T.W. & Ibrahim, M.B., Measurements, computation and analysis of a semi-constrained axisymmetric impinging jet, ASME paper GT2004-54215, 2004.
[21] Kercher, D.M. & Tabakoff, W., Heat transfer by a square array of round air jets impinging perpendicular to a flat surface including the effect of spent air. *Journal of Engineering for Power*, **92**, pp. 73–82, 1970.
[22] Metzger, D.E., Florschuetz, L.W., Takeuchi, D.I., Behee, R.D. & Berry, R.A., Heat transfer characteristics for inline and staggered arrays of circular jets with cross flow of spent air. *Journal of Heat Transfer*, **101**, pp. 526–531, 1979.
[23] Florschuetz, L.W., Truman, C.R. & Metzger, D.E., Streamwise flow and heat transfer distributions for jet array impingement with cross flow. *Journal of Heat Transfer,* **103**, pp. 337–342, 1981.
[24] Park, J., Goodro, M., Ligrani, P., Fox, M. & Moon, H., Separate effects of Mach number and Reynolds number on jet array impingement heat transfer. *Journal of Turbomachinery*, **129**, pp. 269–280, 2007.
[25] Kanokjaruvijit, K. & Martinez-Botas, R.F., Parametric effects on heat transfer of impingement on dimpled surface. *Journal of Turbomachinery*, **127**, pp. 287–296, 2005.
[26] Chupp, R.E., Helms, H.E., McFadden, P.W. & Brown, T.R., Evaluation of internal heat transfer coefficients for impingement cooled turbine blades. *Journal of Aircraft*, **6(1)**, pp. 203–208, 1969.

[27] Bunker, R.S. & Metzger, D.E., Local heat transfer in internally cooled turbine airfoil leading edge regions: Part I – Impingement cooling without film coolant extraction. *Journal of Turbomachinery*, **112**, pp. 451–458, 1990.
[28] Metzger, D.E. & Bunker, R.S., Local heat transfer in internally cooled turbine airfoil leading edge regions: Part II – Impingement cooling with film coolant extraction. *Journal of Turbomachinery*, **112**, pp. 459–466, 1990.
[29] Chyu, M.K., Hsing, Y.C. & Natarajan, V., Heat transfer on the base surface of three-dimensional protruding elements. *International Journal of Heat and Mass Transfer*, **39(4)**, pp. 2925–2935, 1996.
[30] Uzol, O. & Camci, C., Elliptical pin fins for gas turbine blade cooling applications. Part 2: Wake flow field measurements and visualization using particle image velocimetry, ASME paper 2001-GT-181, 2001.
[31] Mahmood, G.I., Won, S.Y. & Ligrani, P.M., Local Nusselt numbers and flow structure in a rectangular channel with cylindrical pin-fins, Department of Mechanical Engineering, University of Utah, Salt Lake City, UT, 2002.
[32] Ligrani, P.M., Oliveira, M.M. & Blaskovich, T., Comparison of heat transfer augmentation techniques. *AIAA Journal*, **41(3)**, pp. 337–362, 2003.
[33] Chyu, M.K. & Natarajan, V., Heat transfer on the base surface of three-dimensional protruding elements. *International Journal of Heat and Mass Transfer,* **39(14)**, pp. 2925–2935, 1996.
[34] Ligrani, P.M. & Mahmood, G.I., Variable property Nusselt numbers in a channel with pin fins. *Journal of Thermophysics and Heat Transfer,* **17(1)**, pp. 103–111, 2003.
[35] Metzger, D.E., Berry, R.A. & Bronson, J.P., Developing heat transfer in rectangular ducts with staggered arrays of short pin fins. *Journal of Heat Transfer*, **104**, pp. 700–706, 1982.
[36] Kays, W.M., Crawford, M.E. & Weigand, B., *Convective Heat and Mass Transfer*, McGraw-Hill Book Company, Inc.: New York, 2005.
[37] Gebhart, B., *Heat Transfer*, McGraw-Hill Book Company, Inc.: New York, 1961.
[38] Incropera, F.P. & DeWitt, D.P., *Fundamental of Heat and Mass Transfer*, 5th edn, John Wiley and Sons: Hoboken, NJ, 2002.
[39] Lezius, D.K. & Johnston, J.P., Roll-cell instabilities in rotating laminar and turbulent channel flows. *Journal of Fluid Mechanics*, **77(**part 1), pp. 153–175, 1976.
[40] Wagner, J.H., Johnson, B.V. & Kopper, F.C., Heat transfer in rotating serpentine passages with smooth walls. *Journal of Turbomachinery*, **113**, pp. 321–330, 1991.
[41] Casarsa, L. & Arts, T., Experimental investigation of the aerothermal performance of a high blockage rib-roughened cooling channel. *Journal of Turbomachinery*, **127**, pp. 580–588, 2005.
[42] Kiml, R., Mochizuki, S. & Murata, A., Effects of rib arrangements on heat transfer and flow behavior in a rectangular rib-roughened passage: application to cooling of gas turbine blade trailing edge. *Journal of Heat Transfer*, **123**, pp. 675–681, 2001.

[43] Fu, W.L., Wright, L.M. & Han, J.C., Heat transfer in two-pass rotating rectangular channels (AR = 1:2 and AR = 1:4) with 45 degree angled rib turbulators. *Journal of Heat Transfer*, **127**, pp. 164–174, 2005.
[44] Wright, L.M., Fu, W.-L. & Han, J.-C., Thermal performance of angled, V-shaped, and W-shaped rib turbulators in rotating rectangular cooling channels (AR = 4:1). *Journal of Turbomachinery*, **126**, pp. 604–614, 2004.
[45] Griffith, T.S., Al-Hadhrami, L. & Han, J.C., Heat transfer in rotating rectangular cooling channels (AR = 4) with dimples. *Journal of Turbomachinery*, **125**, pp. 555–564, 2003.
[46] Burgess, N.K., Oliveira, M.M. & Ligrani, P.M., Nusselt number behavior on deep dimples surfaces within a channel. *Journal of Heat Transfer*, **125**, pp. 11–18, 2003.
[47] Mahmood, G.I., Hill, M.L., Nelson, D.L., Ligrani, P.M., Moon, H.-K. & Glezer, B., Local heat transfer and flow structure on and above a dimpled surface in a channel. *Journal of Turbomachinery*, **123**, pp. 115–123, 2001.
[48] Kreith, F. & Bohn, M.S., *Principles of Heat Transfer,* Brooks/Cole: Pacific Grove, CA, 2000.
[49] Incropera, F.P. & DeWitt, D.P., *Fundamentals of Heat and Mass Transfer,* John Wiley & Sons: New York, NY, 2001.
[50] Jiang, N. & Simon, T.W., Modeling laminar-to-turbulent transition in a low-pressure turbine flow which is unsteady due to passing wakes: Part I – Transition onset, ASME paper GT2003-38787, 2003.
[51] Mayle, R.E., The role of laminar-turbulent transition in gas turbine engines. *Journal of Turbomachinery,* **113**, pp. 509–537, 1991.
[52] Van Fossen, G.J., Simoneau, R.J. & Ching, C.Y., Influence of turbulence parameters, Reynolds number, and body shape on stagnation-region heat transfer. *Journal of Heat Transfer,* **117**, pp. 597–603, 1995.
[53] Tennekes, H. & Lumley, J.L., *A First Course in Turbulence,* The MIT Press: Cambridge, MA, 1972.
[54] Giel, P.W., Boyle, R.J. & Bunker, R.S., Measurements and predictions of heat transfer on rotor blades in a transonic turbine cascade. *Journal of Turbomachinery*, **126(1)**, pp. 110–121, 2004.
[55] Van Fossen, G.J. & Bunker, R.S., Augmentation of stagnation region heat transfer due to turbulence from a DLN (dry low-NO_x) can combustor, ASME paper 2000-GT-215, 2000.
[56] Bunker, R.S., Personal communication, 2007.
[57] Dullenkopf, K. & Mayle, R.E., An account of free-stream-turbulence length scale on laminar heat transfer. *Journal of Turbomachinery*, **117**, pp. 401–406, 1995.
[58] Rued, K. & Wittig, S., Laminar and transitional boundary layer structures in accelerating flow with heat transfer, ASME paper 86-GT-97, Dusseldorf, Germany, 1986.
[59] Patankar, S., *Numerical Heat Transfer and Fluid Flow*, Hemisphere Publishing Corp.: New York, NY, 1980.
[60] Fluent Users' Manual: http://jullio.pe.kr/fluent6.1/help/html/ug/main_pre.htm

[61] Star-CD web site: http://www.cd-adapco.com/products/STAR-CD/index.html
[62] CFX web site: http://www.ansys.com/products/cfx.asp
[63] Durbin, P., Near wall turbulence closure modeling without 'damping functions,' *Theoretical Computational Fluid Dynamics*, **3(1)**, pp. 1–13, 1991.
[64] Dunn, M.G., Convective heat transfer and aerodynamics in axial flow turbines. *Journal of Turbomachinery*, **123**, pp. 637–686, 2001.
[65] Abhari, R.S. & Epstein, A.H., An experimental study of film cooling in a rotating transonic turbine, ASME paper 92-GT-201, 1992.
[66] Giel, P.W., Van Fossen, G.J., Boyle, R.J., Thurman, D.R. & Civinskas, K.C., Blade heat transfer measurements and predictions in a transonic turbine cascade, ASME paper 99-GT-125, 1999.
[67] Langston, L.S., Crossflow in a turbine cascade passage. *Journal of Engineering for Power*, **10**, pp. 866–874, 1980.
[68] Goldstein, R.J., Wang, P.H. & Jabbari, M.Y., The influence of secondary flows near the endwall and boundary layer disturbance on convective transport from a turbine blade. *Journal of Turbomachinery*, **117**, pp. 657–663, 1995.
[69] Graziani, R.A., Blair, M.F., Taylor, J.R. & Mayle, R.E., An experimental study of endwall and airfoil surface heat transfer in a large scale turbine blade cascade. *Journal of Engineering for Power*, **102**, pp. 257–267, 1980.
[70] Key, N. & Arts, T., Comparison of turbine tip leakage flow for flat tip and squealer tip geometries at high-speed conditions. *Journal of Turbomachinery*, **128**, pp. 213–220, 2006.
[71] Metzger, D.E. & Rued, K., The influence of turbine clearance gap leakage on passage velocity and heat transfer near blade tips: Part I – Sink flow effects on blade pressure side. *Journal of Turbomachinery*, **111**, pp. 284–292, 1989.
[72] Rued, K. & Metzger, D.E., The influence of turbine clearance gap leakage on passage velocity and heat transfer near blade tips: Part II – Source flow effects on blade suction sides. *Journal of Turbomachinery*, **111**, pp. 293–300, 1989.
[73] Van Fossen, G.J. & Simoneau, R.J., Stagnation region heat transfer: the influence of turbulence parameters, Reynolds number and body shape. *General Papers in Heat and Mass Transfer, Insulation, and Turbomachinery*, eds S.H. Chan, I.S. Habib, L.E. Hochreiter, R.L. Mahajan, E.V. McAssey, J.Y. Murthy, M.S. Sohal, R.J. Couvillion, W.B. Krause, R.S. Amano & R.H. Pletcher, ASME HTD-Vol. 271, 1994.
[74] Saha, A.K., Mahmood, G.I. & Acharya, S., The role of leading-edge contouring on end-wall flow and heat transfer: computations and experiments, ASME paper GT2006-91318, 2006.
[75] Bons, J., Taylor, R., McClain, S. & Rivir, R., The many faces of turbine surface roughness. *Journal of Turbomachinery*, **123**, pp. 739–748, 2001.
[76] Wammack, J.E., Crosby, J., Fletcher, D., Bons, J.P. & Fletcher, T.H., Evolution of surface deposits on a high pressure turbine blade, Part I: Physical characteristics, ASME paper GT2006-91246, 2006.
[77] Bons, J.P., Wammack, J.E., Crosby, J., Fletcher, D. & Fletcher, T.H., Evolution of surface deposits on a high pressure turbine blade, Part II: Convective heat transfer, ASME paper GT2006-91257, 2006.

[78] Bogard, D., Schmidt, D. & Tabbita, M., Characterization and laboratory simulation of turbine airfoil surface roughness and associated heat transfer. *Journal of Turbomachinery*, **120**, pp. 337–342, 1998.
[79] Barlow, D., Kim, Y. & Florschuetz, L., Transient liquid crystal technique for convective heat transfer on rough surfaces. *Journal of Turbomachinery,* **119**, pp. 14–22, 1997.
[80] Goldstein, R.J., Eckert, E.R.G., Chiang, H.D. & Elovic, E., Effect of surface roughness on film cooling performance. *Journal of Engineering for Gas Turbines and Power*, **107(1)**, pp. 111–116, 1985.
[81] Taylor, R., Scaggs, W. & Coleman, H., Measurement and prediction of the effects of nonuniform surface roughness on turbulent flow friction coefficients. *Journal of Fluids Engineering*, **110**, pp. 380–384, 1998.
[82] Turner, A., Hubbe-Walker, S. & Bayley, F., Fluid flow and heat transfer over straight and curved rough surfaces. *International Journal of Heat and Mass Transfer*, **43**, pp. 251–262, 2000.
[83] Hoffs, A., Drost, U. & Bolcs, A., Heat transfer measurements on a turbine airfoil at various Reynolds numbers and turbulence intensities including effects of surface roughness, ASME paper 96-GT-169, 1996.
[84] Bunker, R.S., Separate and combined effects of surface roughness and turbulence intensity on vane heat transfer, ASME paper 07-GT-135, 1997.
[85] Maciejewski, P.K. & Moffat, R.J., Heat transfer with very high free-stream turbulence Part I: Experimental data. *Journal of Heat Transfer*, **114**, pp. 827–833, 1992.
[86] Maciejewski, P.K. & Moffat, R.J., Heat transfer with very high free-stream turbulence Part II: Analysis of results. *Journal of Heat Transfer*, **114**, pp. 834–839, 1992.
[87] Ames, F.E., The influence of large-scale high-intensity turbulence on vane heat transfer. *Journal of Turbomachinery*, **119**, pp. 23–30, 1997.
[88] Garg, V.K., Heat transfer on a film-cooled rotating blade. *International Journal of Heat and Fluid Flow*, **21**, pp. 134–145, 2000.
[89] Librizzi, J. & Cresci, R.J., Transpiration cooling of a turbulent boundary layer in an axisymmetric nozzle. *AIAA Journal*, **2**, p. 617, 1964.
[90] Mick, W.J. & Mayle, R.E., Stagnation film cooling and heat transfer including its effect within the hole pattern. *Journal of Turbomachinery*, **110**, pp. 66–72, 1998.
[91] Burd, S.W. & Simon, T.W., Measurements of discharge coefficients in film cooling. *Journal of Turbomachinery*, **121(2)**, pp. 243–248, 1999.
[92] Gritsch, M., Schulz, A. & Wittig, S., Adiabatic wall effectiveness measurements of film cooling holes with expanded exits. *Journal of Turbomachinery*, **120**, pp. 549–556, 1998a.
[93] Hay, N. & Lampard, D., Discharge coefficient of turbine cooling holes: a review, ASME paper 96-GT-492, 1996.
[94] Friedrichs, S., Hodson, H.P. & Dawes, W.N., Distribution of film cooling effectiveness on a turbine endwall measured using the ammonia and diazo technique. *Journal of Turbomachinery*, **118**, pp. 613–621, 1996.